NATURAL ENVIRONMENT NEAR THE SUN/EARTH-MOON L2 LIBRATION POINT

Prepared for the NEXT GENERATION SPACE TELESCOPE PROGRAM

Steven W. Evans, Editor
Marshall Space Flight Center
MSFC, Alabama

FORWARD

The natural environment near the L2 libration point is characterized by many complex, variable, and frequently subtle processes – more than can be adequately treated in a general description such as this. In many cases the characteristics and interactions among these processes are poorly understood, not least because of the want of adequate measurements of phenomena in this distant location. It is impossible to definitively state limiting (e.g., maximum possible) extreme values for some of the environmental parameters discussed here. Likewise, it may not be technically or economically feasible to design a system to withstand an extreme value when it can be defined, if the probability is small that such a value will occur during the mission lifetime. Nevertheless, some effort must be made to maximize system robustness, since a spacecraft placed into an orbit near L2 will be beyond the reach of manned repair or servicing missions for the forseeable future.

For these reasons, good engineering judgment must be exercised in the application of environment data to space vehicle design analyses. When environmental considerations become significant design or cost drivers, environmental specialists should be consulted to assure that the environment was correctly understood and used, and that subtle or infrequent effects – not addressed by the information presented here – are not present in a form that would compromise the vehicle. Questions of spacecraft charging, susceptibility of sensors and electronics to radiation damage, effects of micrometeoroid impacts on critical surfaces and structural elements, stability of the halo orbit, and other questions will need to be addressed as the spacecraft design matures. However, such questions need to be raised as early as possible in the design process in order to maintain an economical program and obtain a vehicle having minimal operational sensitivity to the environment.

Questions or requests for assistance in the application and extension of the natural environment models described here should be addressed to the Space Environments Team, Environments Group, Engineering Systems Department, Engineering Directorate, Marshall Space Flight Center, AL 35812.

Table of Contents

VII.   Meteoroid Environment   54 – 60

NATURAL ENVIRONMENT NEAR
THE SUN/EARTH-MOON
L2 LIBRATION POINT

Prepared for the
NEXT GENERATION
SPACE TELESCOPE PROGRAM

I. SCOPE AND PURPOSE

The purpose of this document is to provide definitions of the natural environment in the vicinity of the L2 libration point of the Sun/Earth-Moon system, for use in development of the Next Generation Space Telescope (NGST). The L2 point is located approximately 1.5 million kilometers in the anti-sunward direction along the line joining the Sun and the center of mass (barycenter) of the Earth-Moon system. The natural environment in this region of space includes the gravitational fields due to the Earth, Moon, Sun, and planets; plasma, magnetic fields, and energetic charged particles of the solar wind; plasma, magnetic fields, and energetic charged particles of the Earth's magnetospheric tail; shocked plasma, magnetic fields, and energetic charged particles of the magnetosheath between the free solar wind and the magnetospheric tail; galactic cosmic rays; electromagnetic radiation and thermal conditions due to the Sun; and meteoroids, with components due to the sporadic background and to streams.

In its transfer to the vicinity of L2 the NGST will pass through environments from low Earth orbit (LEO), through geosynchronous altitude (GEO), and past the lunar distance; however, the current version of this document does not treat these transfer regimes. Neither does it treat the induced environments and other effects resulting from the presence of the spacecraft itself. These induced effects must however be considered to produce a sound design. This document does not provide techniques or engineering solutions to permit operation in the natural environments described herein.

1.1 Format and Use of the Document

Each section of this document contains an explanation and description of the natural environment characteristic to which it is devoted. The environment descriptions include either nominal or extreme design values of the various parameters, and should be sufficient for general design purposes. If NGST systems exhibit sensitivities to specific parameters that cannot be readily accommodated within the planned system design, designers should contact personnel of the Environments Group, Marshall Space Flight Center (MSFC), AL 35812.
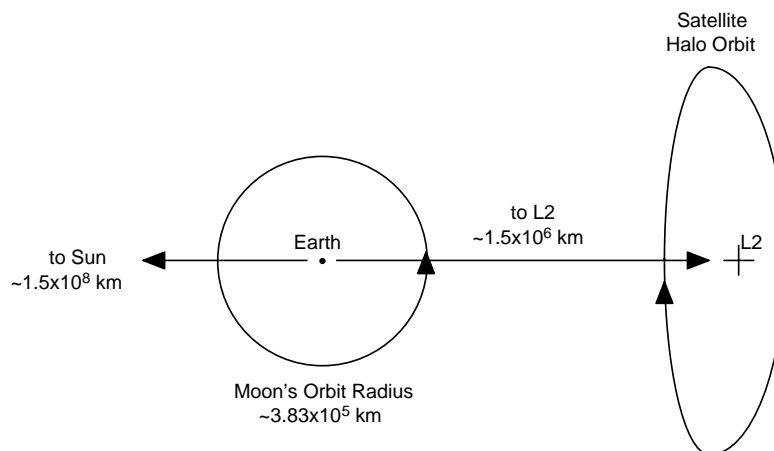
Figure 1.1 General view of Earth-Moon space and L2, with typical halo orbit.

II. GENERAL INFORMATION

This section provides frequently used physical constants and describes the general character of the space environment near L2.

2.1 Constants for the Sun, Earth, and Moon

The values given in Table 2.1 define parameters for use in NGST design performance analyses. Sources of the data are given as numbered references.

Table 2.1 Sun, Earth, and Moon Physical Constants

Mean distance to the Sun	=	1.4959787×10^8 km, or 1 Astronomical Unit (AU)	[1]
Solar constant	=	1367 ± 10 W/m^2 at 1 AU 1340 ± 10 W/m^2 at L2	[2]
Mean synodic solar rotation period	=	27.2753 d at the equator	[3]
Solar radiation pressure (100% reflecting, normal incidence)	=	9.12×10^{-6} N/m^2 at 1 AU 8.94×10^{-6} N/m^2 at L2	[4]
Space sink temperature	=	7 K	[5]
Earth heliocentric eccentricity	=	0.016708158	[3]
Earth heliocentric sidereal period	=	365.25636 mean solar days	[3]
Moon orbit semimajor axis	=	384,400 km	[3]
Moon orbit eccentricity	=	0.054900489	[3]
Moon orbit inclination to ecliptic	=	5.1453964 deg	[3]
Moon orbit sidereal period	=	27.321662 mean solar days	[3]
Earth gravitational parameter, GM_{Earth}	=	398600.4418 km^3/s^2	[6]
Earth equatorial radius, R_E	=	6378.1370 km	[6]
Earth angular rate	=	7.292115×10^{-5} radians/s	[6]
Obliquity of Earth equator to ecliptic	=	23.44 deg	[3]
Moon gravitational parameter, GM_{Moon}	=	4902.8104 km^3/s^2	[6]
Moon equatorial radius, R_M	=	1737.95 km	[6]
Distance from center of Earth to Earth-Moon barycenter	=	4670.731 km (calculated from other table entries)	

Distance from Earth-Moon barycenter
  to L2 libration point (varies due to
    eccentricity of Earth-Moon
      heliocentric orbit)
	=	$1.5077 \pm 0.0252 \times 10^6$ km
		$(0.010078 \pm 0.000168$ AU)
		$(236.4 \pm 4.0$ $R_E)$
			[7]

2.2 Overview of Characteristics of the L2 Environment

The L2 libration point is a position of unstable equilibrium in the gravitational system consisting of the Sun and the Earth-Moon system. In general a spacecraft in an orbit about the Sun whose radius is greater than that of the Earth's will move at a slower angular rate with respect to the stars than the Earth does, i.e., its period will be longer and it will 'fall behind' as viewed from the Earth. However, at L2 the added gravitational attraction provided by the Earth and Moon will accelerate the spacecraft's motion, allowing it to keep pace with them in their course about the Sun. As one might expect this balance of forces is a delicate one, and perturbations due to the motion of the Earth and Moon about their barycenter, due to the eccentricity of the Earth-Moon system's heliocentric orbit, due to passing planets, and due to the radiation pressure of the ambient sunlight may nudge the spacecraft away from the equilibrium position and send it drifting off into an independent heliocentric orbit. In practice the spacecraft will be placed into a 'halo' orbit about the nominal equilibrium point, and it must be maintained in this halo orbit by periodic station-keeping maneuvers to compensate for the perturbations. In the case of the NGST the radiation pressure accelerations are likely to be substantial, due to its large sunshield; it may be possible to design the vehicle's control system to make use of these accelerations in performing the needed correction maneuvers, thus conserving propellant. The effects of the solar radiation pressure could also be minimized by biasing the halo orbit.

A spacecraft in an L2 halo orbit will be subject to the ambient plasma and ionizing radiation environments due to both the solar wind and the geomagnetic tail. L2 lies approximately 236 Earth radii, R_E (a commonly-used distance increment in space plasma work), beyond the Earth-Moon barycenter, and halo orbits of the type considered for NGST typically occupy volumes on a scale of 40 by 60 by 200 R_E with the long axis oriented along the direction of heliocentric orbital motion. At the L2 distance the geotail is approximately 45 to 70 R_E in diameter, depending on the solar wind dynamic pressure. Its centerline can shift by some 40 R_E, depending on the direction of the solar wind. Therefore a spacecraft in an L2 halo orbit may be immersed in the tail some of the time, immersed in the free solar wind some of the time, and inside the shocked plasma of the magnetosheath between these regions the rest of the time. Within the geotail, the spacecraft will be subject to the different plasma regimes of its complex structure. The spacecraft will require careful design to operate within this extremely dynamic plasma environment without damage from discharge events, contamination, interference with communication and other electronic hardware, and other effects. The solar wind and geotail plasmas are composed primarily of electrons and protons, with an admixture of alpha particles at about 4.7% the number of protons.

The NGST will be subject to the effects of energetic particles produced by the Sun, the geotail, and the galactic cosmic ray (GCR) background. This energetic particle flux, also known as ionizing radiation, can cause several types of damage, including Single Event Upsets (SEU) to electronic memory and logic components; changes in material and electronic properties due to Total Ionizing Dose (TID) from cumulative penetrations; and changes in the transmission and reflection properties of optical components. GCR particles are electrons and positively charged ions, the latter consisting of protons (85%), alphas (14%), and heavier ions (1%). The main detrimental effect of GCR is production of SEU's. The most important ionizing radiation component from a spacecraft operations perspective will be the intense particle fluxes produced by solar ejection events. During these events the solar ion fluxes can exceed the GCR background by factors of 10^3 to 10^4 for short periods. This adds substantially to the TID and may cause SEU's.

The spacecraft will be exposed to the full spectrum of electromagnetic energy produced by the Sun. As described in detail in Section 6, the solar spectrum can be approximated by the output of a blackbody at 5777 K, with an integrated power of 1367 W/m^2 at 1 AU, as given in Table 2.1. The thermal regime will be controlled by the balance between absorbed solar energy and the ability of the spacecraft to radiate this energy into deep space. In this regard the integrity of the sunshield will be of tremendous importance in determining whether the NGST telescope can reach and maintain its desired operating temperature range (see the discussion below on the meteoroid environment). Electromagnetic noise produced by terrestrial sources will be of negligible importance at L2. However, the radio noise produced by the Sun can interfere with uplink communications if the line of sight from the spacecraft to the Earth is

too close to the spacecraft-Sun line. This is one constraint on the choice of the halo orbit: it should be large enough to eliminate this communication problem. The typical orbit mentioned above would have a minimum Sun-Earth angle of approximately 4.3 deg, which may or may not provide a sufficient angular separation to avoid problems. The intensity of solar electromagnetic emission, the level of production of solar ionizing radiation, the speed and density of the solar wind, and the strength of the solar magnetic field all vary more or less cyclically with an average period of 11 years. The exact level of solar activity cannot be predicted very accurately, although the phase within a given activity cycle can be established. Energetic particles, radio noise, plasma streams, and intense ultraviolet and X-ray radiation tend to be emitted from localized regions on the Sun's surface. These localized active regions and some coronal features persist longer than the mean solar rotation period of 27 days, and since they only affect near-Earth space when they face us, enhanced solar activity can be estimated 27 or more days in advance [1].

Spacecraft at L2 will be subject to bombardment by meteoroids, but owing to the limited and transient residence of manmade objects in this region, artificial space debris should not pose a collision hazard for many years. Meteoroids are classified either as members of the sporadic population or as members of identified streams. The sporadic meteoroids are found to appear from six radiants, or apparent source directions in space, related to the motion of the observer about the Sun. They are observed with uniform frequency throughout the year. No specific parent bodies for these mobile radiants are known, but dynamical studies have demonstrated that the particles emanating from the four radiants in or near the ecliptic plane are products of long-period and short-period comets. Conversely, parent comets *have* been identified for many meteoroid streams, which are clouds of particles scattered along and near the orbits of their parent bodies after having been ejected from them. Stream meteoroids are observed during regular intervals when the Earth cuts through the volumes of space traversed by these particles. The materials, spacing, design geometry, and other characteristics of the NGST sunshield must be carefully examined and tested in order to meet the expected meteoroid bombardment and still maintain the spacecraft's necessary thermal conditions. Also, the effects of meteoroid impacts on the NGST mirror must be carefully investigated.

In the subsequent sections of this document the environment characteristics briefly covered here will be treated in much greater detail.

References:

[1] Anderson, B. Jeffrey, Ed., Robert E. Smith, Compiler, *Natural Orbital Environment Guidelines for Use in Aerospace Vehicle Development*, NASA Technical Memorandum 4527, Marshall Space Flight Center, June 1994.

[2] Kasten, F. and C. G. Justus*, Solar Spectral Irradiance*, International Illumination Commission (CIE) Publication 85, CIE TC2-17 Committee, 1989.

[3] *The Astronomical Almanac*, U. S. Government Printing Office, 1990.

[4] Geyling and Westerman, *Introduction to Orbital Mechanics*, Addison-Wesley, 1971.

[5] Perrygo, C., *personal communication*, May 2000.

[6] *World Geodetic System 84, Earth Gravity Model 96*, National Imagery and Mapping Agency.

[7] Richardson, David L., "Analytical Construction of Periodic Orbits About the Collinear Points," Celestial Mechanics **22**, 241-253, 1980.

III. GRAVITATIONAL FIELDS AND PERTURBATIONS

The NGST will be placed in the vicinity of a point of unstable equilibrium, known as "L2," in the Sun/Earth-Moon dynamical system, which is modeled by the classical Circular Restricted Three-Body Problem described in Section 3.1. In this model we consider the Earth and the Moon as a single body, called the Earth-Moon, taken as a point mass at the Earth-Moon barycenter. Neglecting the Moon would cause too great an error in the Three-Body model (Sun/Earth/Spacecraft), while treating the Sun/Earth/Moon/Spacecraft in a Four-Body Problem would make the model too complex for analysis. The Sun/Earth-Moon Three-Body model has proven to be more than adequate for mission design and analysis.

Because the equilibrium at L2 is unstable, small perturbations acting over time can cause the spacecraft trajectory to depart from the desired volume of space and enter an unrestricted heliocentric orbit. Section 3.2 describes the gravitational perturbations in the L2 vicinity due to various planetary bodies in the Solar System. In this treatment all bodies are considered to be gravitational point sources. A non-gravitational natural perturbation of importance for NGST will be that due to solar radiation pressure, which is discussed in Section 3.3.

3.1 The Circular Restricted Three-Body Problem (CRTBP)

If we consider the motion of an object with infinitesimal mass, such as a spacecraft, in the gravitational field of two massive bodies revolving about their common center of mass (barycenter) in circular orbits, we have a case of the "Circular Restricted Three-Body Problem." The problem is known as "restricted" because the small body does not influence the motion of the massive bodies. The geometry of this problem is shown in Figure 3.1. Here the two massive bodies, or primaries, are located on the X-axis of a reference frame co-rotating with their motion, with the origin of coordinates at their barycenter. A well-known result in celestial mechanics, due to Euler and Lagrange, is that there are five locations in this rotating reference frame in the plane of motion of the large bodies, at which the small body may be placed and be in dynamical equilibrium. These locations are marked in the figure as L1 – L5. The colinear equilibrium points L1, L2, and L3 lie on the X-axis, while L4 and L5 form equilateral triangles with the primaries. In the Sun/Earth-Moon system, L1 and L2 each lie about 1.5 million km from the Earth.
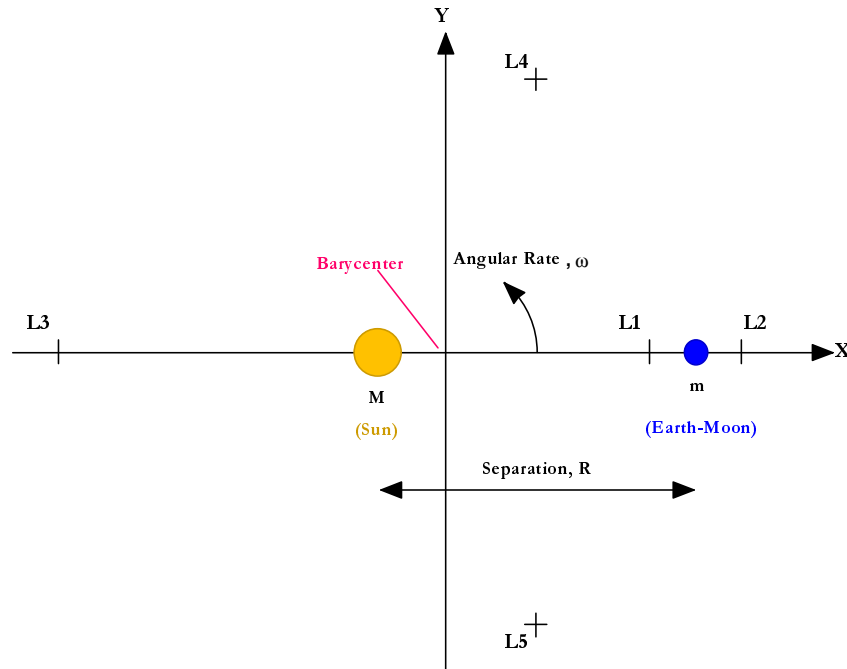

Figure 3.1 Coordinate system and equilibrium points for the Circular Restricted Three-Body Problem.

In the real Solar System, the primaries move on elliptical orbits about their barycenter. The eccentricity of the elliptical motion causes the distance R between the two primaries and their angular rate ω to vary. Also, perturbations due to other planets introduce further small changes in R and ω. We can simplify the mathematical treatment of this system by using the CRTBP if we assume the primaries are moving in circular orbits, and if we change units and approximate the following quantities to be unity: (i) the mean distance between the primaries; (ii) the mean angular rate of the primaries; and (iii) the sum of the masses of the primaries (so that the smaller mass is taken to be 'm' and the larger mass is taken to be '1 – m'). The equations of motion for the CRTBP are [1]:

$$d^2X/dt^2 - 2\ dY/dt = U_X \tag{3.1a}$$

$$d^2Y/dt^2 + 2\ dX/dt = U_Y \tag{3.1b}$$

$$d^2Z/dt^2 \qquad\quad = U_Z \tag{3.1c}$$

where letter subscripts denote the partial derivative with respect to the variable, and

$$U = 1/2\ (X^2 + Y^2) + (1 - m)/d_1 + m/d_2 \tag{3.2a}$$

$$d_1 = [(X - m)^2 + Y^2 + Z^2]^{1/2} \tag{3.2b}$$

$$d_2 = [(X + 1 - m)^2 + Y^2 + Z^2]^{1/2} \tag{3.2c}$$

The linearized equations of motion of the small body are [2]:

$$d^2X/dt^2 - 2\ dY/dt - (2B_{Li} + 1)X = 0 \tag{3.3a}$$

$$d^2Y/dt^2 + 2\ dX/dt + (B_{Li} - 1)Y = 0 \tag{3.3b}$$

$$d^2Z/dt^2 + B_{Li}Z = 0 \tag{3.3c}$$

where

$$B_{L1} = [(1 - m)/(1 - \gamma_{L1})^3 + m/\gamma_{L1}^3] \tag{3.4a}$$

$$B_{L2} = [(1 - m)/(1 + \gamma_{L2})^3 + m/\gamma_{L2}^3] \tag{3.4b}$$

and the parameters γ_{Li}, which give the locations of the equilibrium points with respect to the Earth-Moon, are roots of quintic equations, approximated by

$$\gamma_{L1} = (m/3)^{1/3}\ [1 - (1/3)(m/3)^{1/3} - (1/9)(m/3)^{2/3} + \ldots] \tag{3.5a}$$

$$\gamma_{L2} = (m/3)^{1/3}\ [1 + (1/3)(m/3)^{1/3} - (1/9)(m/3)^{2/3} + \ldots] \tag{3.5b}$$

Values for some of the above quantities for the Sun/Earth-Moon system are:

m	3.0404×10^{-6}	R	1.4960×10^8 km (1.000000 AU)
γ_{L1}	1.0011×10^{-2}	$\gamma_{L1}R$	1.4976×10^6 km (0.010011 AU)
γ_{L2}	1.0078×10^{-2}	$\gamma_{L2}R$	1.5077×10^6 km (0.010078 AU)
B_{L1}	4.0611	$\Delta\gamma_{L1}R$	$\pm 0.0251 \times 10^6$ km (due to eccentricity)
B_{L2}	3.9405	$\Delta\gamma_{L2}R$	$\pm 0.0252 \times 10^6$ km

Motion perpendicular to the X-Y plane is a simple harmonic with frequency $(B_{Li})^{1/2}$. The motion in the X-Y plane is coupled, and the characteristic equation is given by

6

$$s^4 - (B_{Li} - 2)s^2 - (2B_{Li} + 1)(B_{Li} - 1) = 0 \tag{3.6}$$

Inserting the value for B_{L2}, this equation has the roots

$$s_{L2} = \pm 2.4843, \ \pm 2.0570 \, i \tag{3.7}$$

Similar roots exist for L1 and L3. Because positive real roots exist the collinear points are unstable.

3.2 Halo Orbits Near L2

For the equations of motion given above the in-plane and out-of-plane frequencies of the motion about the equilibrium point are not exactly the same, with the result that the satellite describes Lissajou patterns centered on the equilibrium point when viewed from the Earth. This can have adverse consequences for communications, since at times the line of sight from the spacecraft to the Earth comes quite close to the Sun, which generates radio noise. One would prefer that the spacecraft circulate about the libration point in a closed loop, or "halo orbit," of fixed size. Halo-type periodic motion is obtained if the amplitudes of the in-plane and out-of-plane motions are of sufficient magnitude so that the non-linear contributions to the system produce eigenfrequencies that are equal. The linearized solution can then be expressed in the form [2]:

$$X = -A_X \cos(\lambda t + \phi) \tag{3.8a}$$

$$Y = kA_X \sin(\lambda t + \phi) \tag{3.8b}$$

$$Z = A_Z \sin(\lambda t + \psi) \tag{3.8c}$$

In these expressions, the amplitudes A_X and A_Z are constrained by a non-linear algebraic relationship found as a result of the application of the Linstedt-Poincare expansion perturbation method used in developing the problem:

$$l_1 A_X^2 + l_2 A_Z^2 + \Delta = 0 \tag{3.9}$$

where l_1 and l_2 are particular constants, Δ is a correction constant of $O(A_Z^2)$, and A_X and A_Z are expressed as multiples of the distance from the Earth-Moon to the Lagrange point. The multiplicative factor, k, between the X- and Y-amplitudes is found from a relation between the in-plane frequency, λ, and the squared harmonic frequency, B_{Li}:

$$k = (\lambda^2 + 1 + 2B_{Li})/2\lambda \tag{3.10}$$

In addition to this, a phase-angle constraint relationship exists between the in-plane and out-of-plane motions:

$$\psi = \phi + n\pi/2, \quad n = 1,3 \tag{3.11}$$

The set of third-order solutions embodying these constraints and employing frequency corrections to eliminate secular terms is:

$$X = a_{21} A_X^2 + a_{22} A_Z^2 - A_X \cos \tau_1 + (a_{23} A_X^2 - a_{24} A_Z^2) \cos 2\tau_1$$
$$+ (a_{31} A_X^3 - a_{32} A_X A_Z^2) \cos 3\tau_1 \tag{3.12a}$$

$$Y = k A_X \sin \tau_1 + (b_{21} A_X^2 - b_{22} A_Z^2) \sin 2\tau_1 + (b_{31} A_X^3 - b_{32} A_X A_Z^2) \sin 3\tau_1 \tag{3.12b}$$

$$Z = \delta_n A_Z \cos \tau_1 + \delta_n d_{21} A_X A_Z (\cos 2\tau_1 - 3) + \delta_n (d_{32} A_Z A_X^2 - d_{31} A_Z^3) \cos 3\tau_1 \tag{3.12c}$$

where

7

$$\delta_n = 2 - n, \; n = 1,3$$

is a switch function leading to the existence of mirror-image halo orbit solutions as seen in Figure 3.2. The independent variable is

$$\tau_1 = \lambda \, \tau + \phi \, ,$$

τ being a dimensionless time variable chosen to eliminate any secular terms. a_{ij}, b_{ij}, and d_{ij} are constants given in [3]. These equations have been coded into the trajectory simulation portion of the environmental phenomenology code, LRAD, developed to support this environmental definition effort and further described in Chapter IV.

As an example, for the Sun/Earth-Moon system an L2 halo orbit having a Z-amplitude, A_Z, of 125,000 km requires an X-amplitude, A_X, of approximately 215,000 km to produce a periodic halo orbit. The corresponding A_Y is 3.18723 A_X or about 686,000 km. This example halo orbit is shown in Figure 3.2, where L2 is at the origin of coordinates. The period of revolution about this orbit is 180.145 days, so the satellite completes just over two circuits per year. Because these orbits are inherently unstable, station-keeping maneuvers or other techniques are required to maintain them [4].

3.3 Gravitational Perturbation Sources

There are several perturbation sources for a spacecraft at L2 of the Sun/Earth-Moon system. First of all the motion will be disturbed by the motion of the Moon about the Earth. The orbit of the Moon centered at the Earth is inclined to the ecliptic by 5.145 degrees, and the orbital plane precesses with respect to the Sun-barycenter line (X-axis) with a period of 18.613 years [5]. Perturbations vary during this precessional period, with maximum variations about the mean accelerations as shown in Table 3.1. Figure 3.3 presents plots of the perturbations during a typical 28 day Earth-Moon revolution cycle.

Table 3.1 Mean Accelerations and Variations About the Mean from Perturbations
Due to the Earth-Moon System.

Axis	Mean Acceleration (km/s^2)	Maximum Variations (km/s^2)
X	-5.990085×10^{-6} * -1.776141×10^{-7} **	$\pm\, 5.5346 \times 10^{-10}$
Y	0.	$\pm\, 5.8480 \times 10^{-10}$
Z	0.	$\pm\, 0.7017 \times 10^{-10}$

*Acceleration at L2 due to Sun/Earth-Moon, with Earth-Moon barycenter at 1.0 AU exactly.
**Acceleration due to Earth-Moon only.

Other sources of gravitational perturbations are the planets. The perturbations they produce are also periodic, due to their passage relative to the Earth-Moon system in their orbits. X-axis perturbations are greatest when the planets pass the X-Z plane of the rotating frame, while Y-axis perturbations are greatest when the planets are in the first or fourth quadrants of the X-Y plane. Table 3.2 lists maximum single-planet perturbations at L2, and the period between closest approaches of L2 and the planet from year to year, known as the synodic period. Jupiter and Venus are by far the most important planetary perturbers of a spacecraft at L2. Note that the maximum possible sum of planetary perturbations is of the same order of magnitude as the maximum Earth-Moon variations about the mean acceleration at L2.

Class I
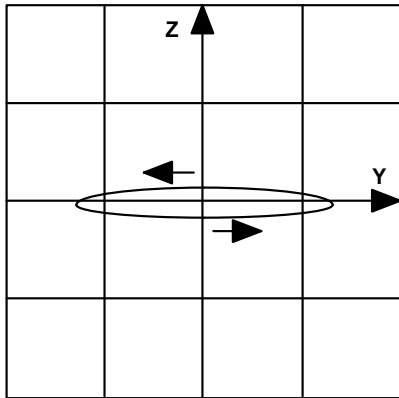
Class II
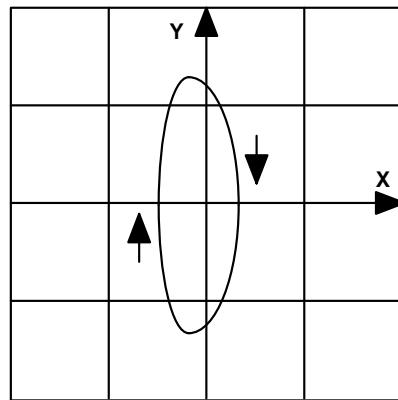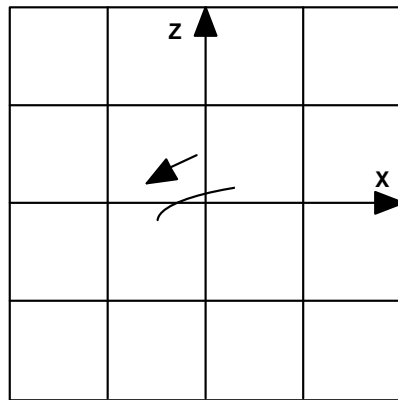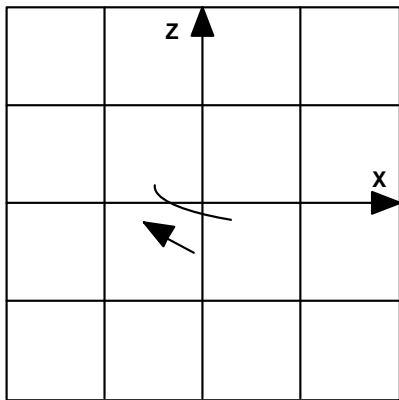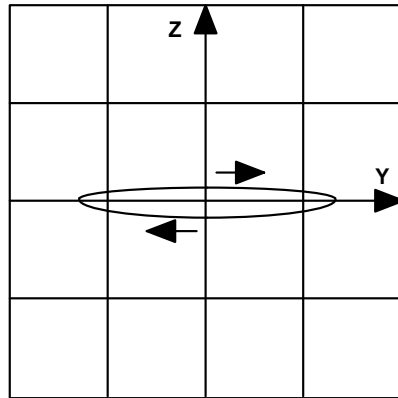
Figure 3.2 Example L2 halo orbit in the Sun/Earth-Moon system. Each division represents 500,000 km.
Z-Amplitude is 125,000 km.
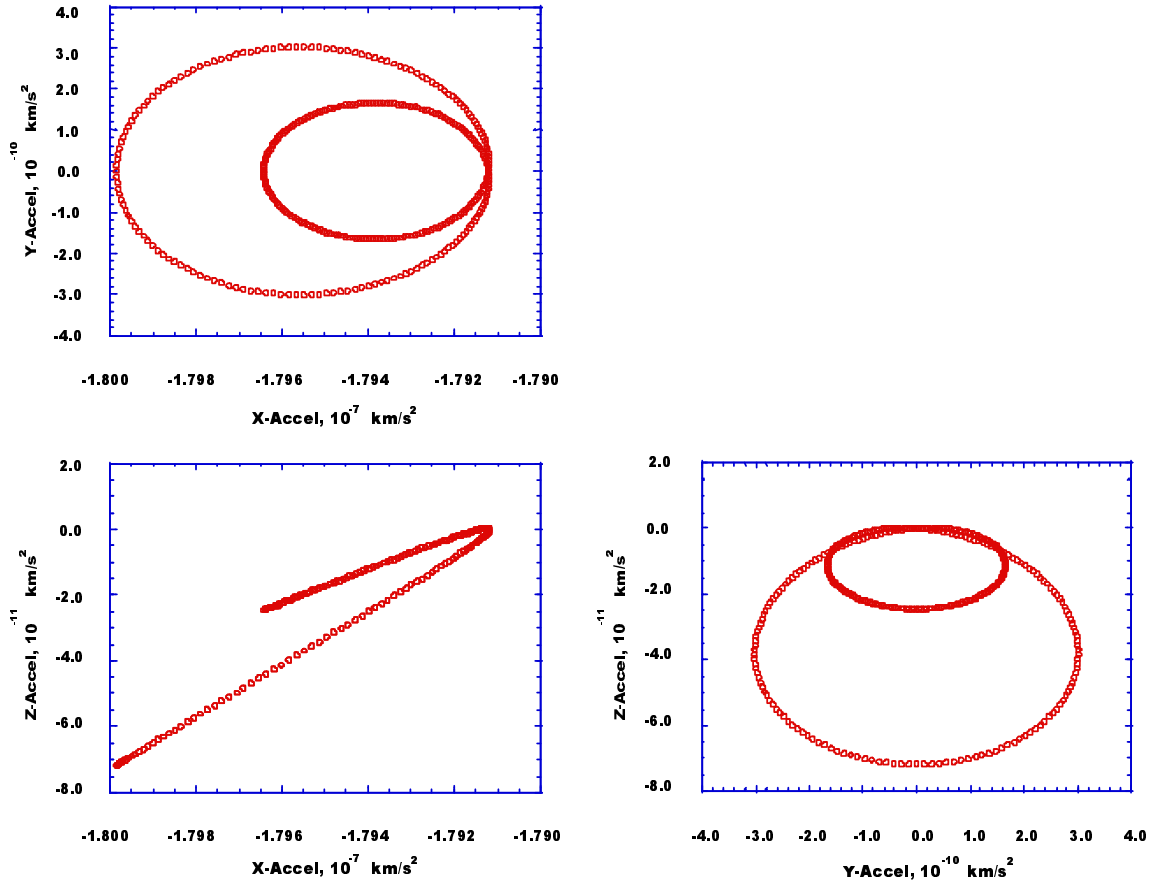
Figure 3.3 Acceleration components during one typical Earth-Moon revolution cycle, as computed at L2.

Table 3.2 Single-Planet Maximum Perturbations and Synodic Periods

Planet	g_{MAX} $(10^{-10}\ km/s^2)$	$g_{MAX}(X)$ $(10^{-10}\ km/s^2)$	$g_{MAX}(Y)$ $(10^{-10}\ km/s^2)$	$g_{MAX}(Z)$ $(10^{-10}\ km/s^2)$	Synodic Period (Days)
Mercury	0.0360	$-\ 0.0360$	$\pm\ 0.0085$	$\pm\ 0.0044$	115.88
Venus	2.0789	$-\ 2.0789$	$\pm\ 0.5972$	$\pm\ 0.1231$	583.92
Mars	0.1529	$+\ 0.1529$	$\pm\ 0.0623$	$\pm\ 0.0049$	779.94
Jupiter	3.6769	$+\ 3.6769$	$\pm\ 2.6124$	$\pm\ 0.0838$	398.88
Saturn	0.2662	$+\ 0.2662$	$\pm\ 0.2169$	$\pm\ 0.0116$	378.09
Uranus	0.0087	$+\ 0.0087$	$\pm\ 0.0078$	$\pm\ 0.0001$	369.66
Neptune	0.0037	$+\ 0.0037$	$\pm\ 0.0035$	$\pm\ 0.0001$	367.48

3.4 Perturbation by Radiation Pressure

The final perturbation source considered here is the radiation pressure due to sunlight falling on the NGST sunshield, and thermal emission from the sunshield. This perturbation has the potential to be turned to advantage in maintaining the spacecraft on station, especially since the sunshield area is expected to be large. The momentum transferred by a photon when it is absorbed by an object is given by

$$p = E/c \qquad\qquad (3.13)$$

where E is the photon energy and c is the speed of light [6]. Typically, instead of photon energy we deal with the radiative flux, Φ, on a surface area. Writing in terms of flux, the pressure exerted on a surface is

$$P = \Phi/c \qquad\qquad (3.14)$$

provided the flux is totally absorbed

Consider the case of specular reflection from a flat surface. If the photon is perfectly reflected back along the direction it came, the momentum transferred is doubled; consequently the reflectivity fraction, k, of the object determines the magnitude of the radiation pressure acceleration. For real surfaces $0 < k < 1$. The acceleration dV/dt (m/s^2), of a mass m (kg), having area A (m^2), and reflectivity k due to the pressure of radiant flux Φ (W/m^2) is given by

$$dV/dt = \Phi\ A\ (1 + k) / m\ c \qquad\qquad (3.15)$$

To examine radiation pressure accelerations at different distances from the Sun, it is convenient to refer to the known flux at 1 AU and make use of the inverse-square decline of radiant energy with distance. At 1 AU the flux is $\Phi_{1AU} = 1367$ W/m^2 (Table 2.1), so if the distance from the Sun is stated in AU and the other units are as above, the radiation pressure acceleration at location R_{AU} is

$$dV/dt = 1367\ (1/R^2{}_{AU}\ )\ A\ (1 + k) / m\ c \qquad (m/s^2) \qquad (3.16)$$

This expression considers only a surface oriented perpendicularly to the radial direction to the Sun. If we consider a surface whose normal is tilted at angle θ to the radial direction ($0 \le \theta < \pi/2$) the acceleration vector will have radial and transverse components (whose unit vectors are **R** and **T**, respectively)

$$d\mathbf{V}/dt = [1367\ A\ \cos(\theta) / m\ R^2{}_{AU}\ c]\ \{[1 + k\ \cos(2\theta)]\ \mathbf{R} + k\ \sin(2\theta)\ \mathbf{T}\} \qquad (3.17)$$

The radial acceleration is greatest when the surface is perpendicular to the radial direction. The transverse acceleration is greatest when θ is approximately 35 deg. For θ beyond about 48 deg the transverse component is greater than the radial, though both are declining rapidly due to the rapid decrease in projected reflector area. Relative component magnitudes are shown in Figure 3.4 for a specularly reflecting flat surface having a reflectivity of 0.9. If NGST pointing capabilities permit, the sunshield could be tilted to the radial direction and the transverse axis aligned in such a way as to allow the radiation pressure acceleration vector to compensate, at least partially, for gravitational perturbations tending to throw the spacecraft off-station. There will always be a non-zero radial acceleration component due to solar radiation pressure if the sunshield is facing the Sun. This can be a significant perturber of the halo orbit for a spacecraft having a large area for its mass. An alternative strategy is to bias the spacecraft trajectory to compensate for the radiation pressure and planetary perturbations [7].

The above discussion considers only specular reflection from a flat surface. In practice the NGST sunshield surface will probably be wrinkled, and reflection from it will include a diffuse component. Also, energy not reflected will be absorbed, heating the sunshield and causing it to radiate.

For a lightly wrinkled surface, with a mean slope error of less than 10 degrees, the amplitude along the primary reflection vector will be reduced less than 2% when compared with reflection off a flat

surface, and the net force will again be parallel to the primary reflection vector [8]. Ideal diffuse reflection is symmetric about the surface normal, and the net force is parallel to the surface normal; significant diffuse reflection would diminish the perturbation correction capabilities of sunshield steering.

Absorption of a portion of the incident sunlight will lead to heating of the sunshield material, and the resulting thermal emissions, and their radiative pressure, will be symmetric about surface normals. By the Stefan – Boltzmann Law the intensity of thermal emission will be proportional to the fourth power of the temperature of the radiating material. Since it is anticipated that the sun-facing side of the sunshield will reach a temperature of about 300 K and it is desired that the rear-most shield surface be no warmer than 80 K, under nominal circumstances the radiant flux from these surfaces should differ by a factor of almost 200. Consequently the net radiant pressure will be symmetric about the sun-facing normal, and will add to the diffuse reflective component in its momentum transfer effect.
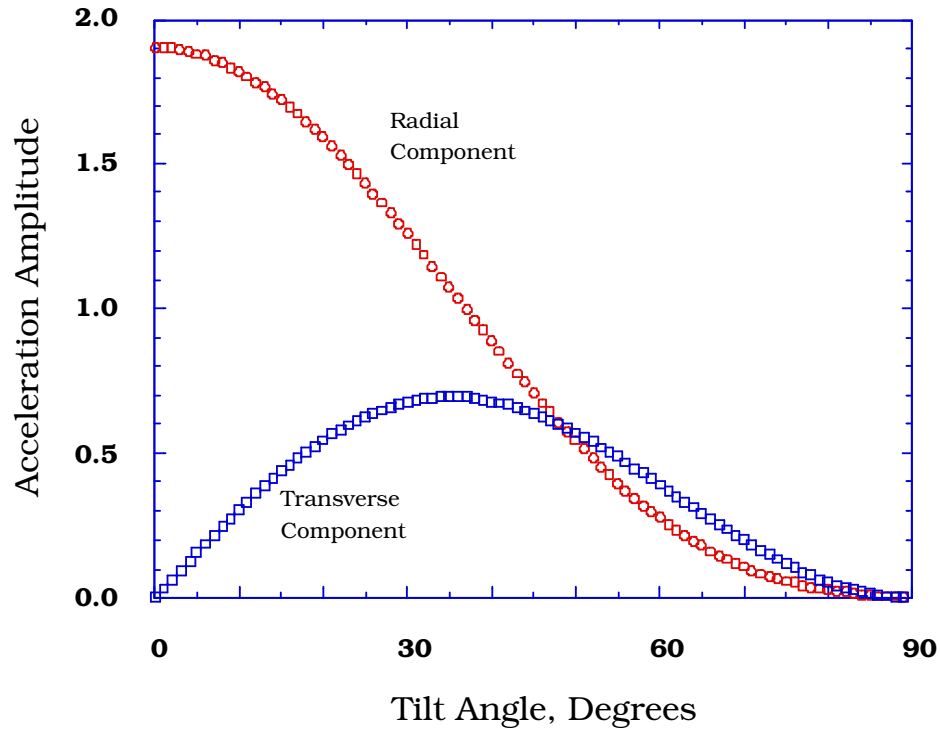
Figure 3.4 Radiation pressure acceleration components as a function of tilt angle of the normal to the reflecting surface with respect to the radial direction to the Sun.

References

[1] Szebehely, Victor, *Theory of Orbits*, Academic Press, 1967.

[2] Farquhar, Robert W., *The Control and Use of Libration-Point Satellites*, NASA Technical Report R-346, Goddard Space Flight Center, Greenbelt, MD, Sept. 1970.

[3] Richardson, David L., "Analytical Construction of Periodic Orbits About the Collinear Points," Celestial Mechanics **22**, 241-253, 1980.

[4] Howell, K. C. and Farquhar, R. W., "John Breakwell, The Restricted Problem, and Halo Orbits," Acta Astronautica, Vol. **29**, No. 6, 485-488, 1993.

[5] *The Astronomical Almanac*, U. S. Government Printing Office, 1990.

[6] Geyling and Westerman, *Introduction to Orbital Mechanics*, Addison-Wesley, 1971.

[7] Bell, J., Wilson, R., Lo, M., "Genesis Trajectory Design," AAS/AIAA Astrodynamics Specialist Conference, Girdwood, AK, August 1999, Paper No. AAS 99-398.

[8] Perrygo, C., *personal communication*, May 2000.

IV. PLASMA ENVIRONMENT

The charged particles treated in this section have energies generally less than a few hundred kilovolts, insufficient to penetrate spacecraft shielding materials. Nonetheless, spacecraft interaction with the plasma environment results in a number of important effects that must be considered in spacecraft design. Plasma primarily affects the external surfaces and structures of a spacecraft, although secondary effects may impact internal systems as well. One example of a primary plasma effect is spacecraft charging due to differential collection of plasma electrons and ions and loss of photoelectrons in the space environment. Severe charging conditions may lead to arcing and re-attraction of contaminant materials to the spacecraft surface. Optical and thermal control system performance may degrade if the charging-enhanced contaminant buildup is severe. Sputtering of material due to impact of energetic ions may alter surface material properties as well, and can be an important consideration in the successful operation of scientific instruments in the solar wind, where ion scouring is required to maintain clean surfaces [1]. Secondary effects due to plasma interactions with the spacecraft may impact internal mechanisms and systems as well. For example, arc discharges can produce electromagnetic interference within spacecraft electronic systems. The material presented in this section provides the necessary plasma parameters required for an assessment of the possible plasma impact on spacecraft design and operation in the L2 plasma environment.

A brief introduction to magnetosphere structure, L2 plasma regimes, and solar wind control of the magnetotail dimensions and orientation are provided in Section 4.1. Mean and limiting values of parameters required to characterize each plasma region are presented in Section 4.2. Statistical values of the particle flux and fluence (time-integrated flux) for a sample halo orbit are given in Sections 4.3 and 4.4, respectively. Directional flux and fluence plots, along with tabular data for each L2 plasma regime, will be provided in appendices to be published as a separate Addendum to this document.

The need to compute particle flux within individual plasma regions, and fluence for complete halo orbits, required development of a new model. This model provides a framework for incorporating statistical variations in plasma parameters and fluctuations in magnetotail structure and position due to time-dependent variations in the solar wind. The model, LRAD, is an engineering-level phenomenology code developed to provide estimates of the plasma environment for satellites in halo orbits about L2. Galactic cosmic ray particles and solar protons are not included in the model. These energetic particles are best considered using standard models, e.g., the CREME and SOLPRO models, which can be implemented independently of LRAD. The discussion of the energetic particle environment is given in Chapter V. Only brief descriptions of the LRAD model and its structure are presented in this chapter. These descriptions should be sufficient to understand the tables and plots of particle flux and fluence. NGST designers should contact the Environments Group, MSFC, if details of the model structure or data analysis techniques used to obtain statistics of the plasma characteristics are required.

Geocentric Solar Ecliptic (GSE) coordinates, a standard system used to order magnetospheric plasma and field observations, are used throughout this chapter. The origin of the GSE coordinate system is the center of the Earth. X_{GSE} and Y_{GSE} axes lie in the ecliptic plane with the X_{GSE} axis pointing towards the Sun along the Earth-Sun line. The Y_{GSE} axis is perpendicular to the X_{GSE} axis and points in the direction opposite the Earth's orbital motion. The Z_{GSE} axis is perpendicular to the ecliptic plane in the direction of the Earth's orbital angular momentum vector, completing the right-handed coordinate system. Distances are commonly given in Earth radii, R_E (6378 km). Note that the X_{GSE} and Y_{GSE} axes in this system point in directions opposite those of the local L2 coordinate system used in Chapter III for describing the halo orbits about L2.

4.1 Magnetosphere Structure, Plasma Regimes, and Magnetotail Dimensions and Orientation

The region of space where plasma properties are mainly controlled by the Earth's magnetic field is known as the magnetosphere. Figure 4.1 illustrates the main features of the near-Earth magnetosphere. The field generated in the Earth's liquid outer core is primarily dipolar and dominates the magnetic topology of the magnetosphere within a few Earth radii. The field is offset from the Earth's center of mass,

and inclined approximately 11 degrees with respect to the rotation axis of the solid Earth. The interaction of the solar wind with the outer regions of the magnetosphere may produce significant perturbations of the
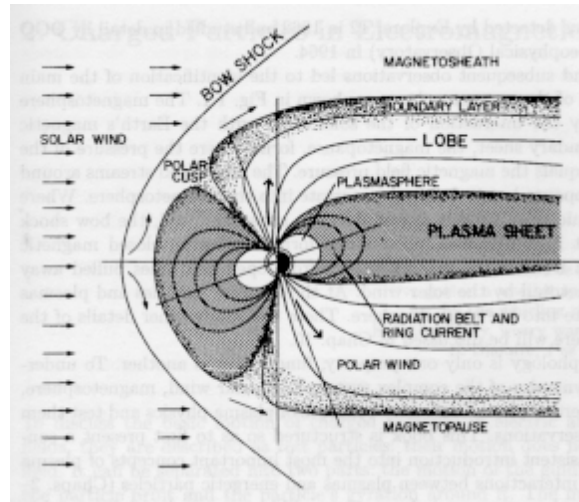

Figure 4.1 Near Earth Magnetosphere. The dipole field, dominant near the Earth, is compressed by the solar wind flow on the day-side and stretched into the extended magnetotail on the night-side of the Earth. This schematic illustrates the main features of the near-Earth ($< 20\ R_E$) magnetosphere in the noon-midnight plane. The plasma sheet, lobes, and boundary layer inside the magnetopause are still identifiable at L2 distances of 236 R_E (from [2]). Note the inclination of the magnetic axis to the rotation axis.

dipolar field. The location of the magnetopause, the outermost boundary of the magnetosphere, is characterized by a current sheet (the "Chapman-Ferraro current") that provides the force balance between the inward-directed dynamic pressure of the external solar wind and the outward-directed stress of the Earth's magnetic field.

The solar wind significantly compresses the geomagnetic field on the day-side of the Earth, and the day-side magnetopause is typically 10-14 R_E from the Earth in the direction of the Sun. Approximately 2 to 3 R_E upstream of the day-side magnetosphere is a shock wave (the "bow shock"), formed where the supersonic solar wind flow is abruptly decelerated upon encountering the magnetosphere. The temperature of the solar wind plasma increases upon traversing the bow shock, as its forward motion is converted to random thermal energy, and its density increases as the plasma stagnates and builds up in front of the magnetosphere in the subsolar region. Plasma in the magnetosheath, the region between the bow shock and the magnetopause, flows around the magnetopause in the same sense as the free solar wind flow.

The L1 point (see Section 3.1) is located approximately 236 R_E sunward of the Earth, well upstream of the magnetopause and bow shock. Satellites at L1 therefore almost exclusively experience only the unperturbed solar wind plasma. Anti-sunward of the Earth, the solar wind interaction stretches the geomagnetic field for at least several hundred Earth radii, forming the extended magnetotail. Magnetotail encounters by satellites have even been reported as far as 500 R_E from the Earth, well past L2.

As shown in Figure 4.2, the magnetic topology of the magnetotail is supported by the neutral sheet, a current sheet flowing from dawn to dusk across the tail. Magnetic field lines in the tail are stretched in the direction of the solar wind flow; they point towards the Earth in the northern lobe of the magnetotail and away from the Earth in the southern lobe, as required by the direction of current flow in the neutral sheet. The hot, dense plasma sheet lies at the center of the tail and includes the neutral sheet, the central plasma sheet, and plasma sheet boundary layers. A boundary layer forms immediately inside the magnetopause due to magnetosheath plasma that enters along open field lines. In the near-Earth magnetosphere the boundary layer contains solar wind plasma that has entered the magnetosphere through the polar cusps (see Fig 4.1). As the boundary layer flows antisunward it also drifts toward the plasma

15

sheet and by some 50 R_E the dominant source of plasma throughout the magnetotail is the solar wind. Inside 50 R_E the ionosphere provides an additional source of plasma to the lobes and plasma sheet. Between the plasma sheet and the magnetopause are the lobes, regions of low density plasma compared to the plasma sheet and magnetosheath.

A cross section illustrating magnetotail plasma regimes is given in Figure 4.3. Many of the distinctions between components of individual regions (i.e., the central plasma sheet, plasma sheet, and plasma sheet boundary layer) are difficult to assign to the L2 plasma environment. However, the main magnetotail regions identified in the near-Earth magnetotail shown in Figure 4.2 are clearly identifiable at L2. These include the boundary layer (including the plasma mantle, lobe, low-latitude boundary layer) and plasma sheet (including the central plasma sheet, boundary plasma sheet, and neutral sheet).
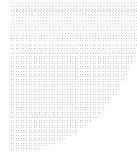
Figure 4.2 Magnetotail Currents. The magnetic field geometry of the magnetotail is produced by a current sheet flowing through the center of the tail and return currents along the magnetopause.

Halo orbits about L2 will typically pass through plasma of the magnetotail, magnetosheath, and free solar wind. Mission designs with large amplitude halo orbits will place the satellite in the relatively high density, low energy plasma of the magnetosheath and solar wind for extended periods of time. In contrast, a mission design with a sufficiently small amplitude halo orbit will place the spacecraft for appreciable times in the relatively low density, high energy plasma of the magnetotail. If halo orbits with amplitudes on the order of the average diameter of the magnetotail are chosen for the mission design, the spacecraft will encounter all of these plasma regions during a single orbit due to the large variability in the cross-secional size, orientation, and actual location of the magnetotail. Characteristic plasma and flow values to be encountered in the halo orbit are described below.

4.2 Magnetosheath and Magnetotail Dimensions and Orientation

4.2.1 Magnetosheath Dimensions

Solar wind interactions with the magnetosphere determine the location of the outer boundary (bow shock) and inner boundary (magnetopause) of the magnetosheath. Because solar wind conditions are variable, magnetosheath dimensions are variable as well. An estimate of the radial distance from the

Earth-Sun line to the bow shock at L2 is ~100 R_E , or 3 to 4 times the average radius of the magnetopause there. This estimate is based on the approximately 85% probability of observing solar wind and magnetosheath plasma regimes by the Geotail satellite given in Plate 1 of Christon et al. [3].
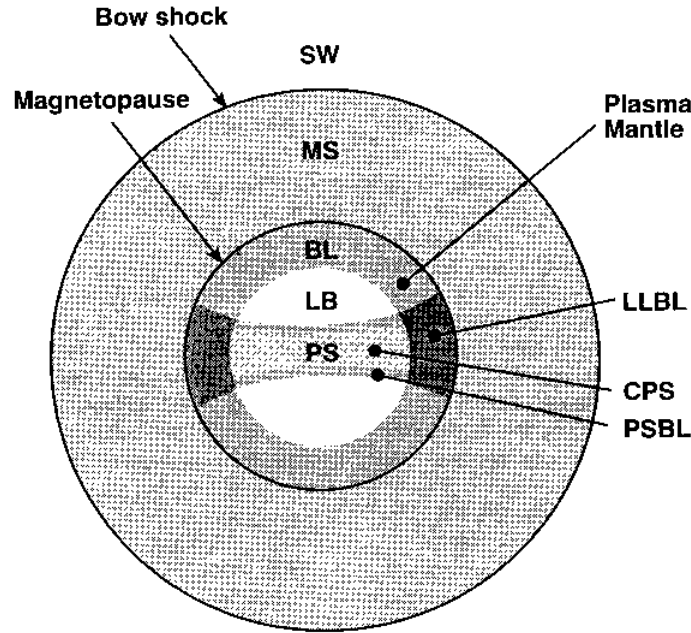
4.3 Schematic of Figure Magnetotail Plasma Regimes. The primary plasma regimes that have been identified in the magnetotail are identified in the Y-Z plane cross section. Labels indicate the plasma sheet (PS), central plasma sheet (CPS), plasma sheet boundary layer (PSBL), low latitude boundary layer (LLBL), lobe (LB), boundary layer or plasma mantle (BL), magnetosheath (MS), and solar wind (SW) [9].

A more sophisticated approach for estimating magnetosheath dimensions, and the one that is incorporated in the LRAD model, is to use the Bennett et al. [4] bow shock and Petrinic and Russell [5,6] magnetopause models. Examples from these models are provided in Figure 4.4. Parameterization of the bow shock and magnetopause locations by magnetic field and plasma characteristics in the solar wind allow the magnetosheath dimensions to be estimated for a variety of solar wind conditions. Note that radial distances to the bow shock from the Sun-Earth line at L2 distance vary as much as 75 R_E. Halo orbits about L2 may therefore place the satellite inside the magnetosheath for extended periods of time.

4.2.2 <u>Magnetotail Dimensions</u>

Estimates of the average radius of the magnetotail have been obtained from ISEE-3 and Geotail satellite observations of plasma and magnetic fields in the vicinity of L2.   Fairfield [6] obtained values ranging from 20 R_E to 30 R_E for a variety of solar wind densities and velocities from ISEE 3 data. Similarly, Christon et al. [3] obtain a value of 25 R_E for the radius by identifying the width of the magnetotail as the interior of the region over which there is a 50% probability of encountering the magnetosheath in Geotail satellite plasma records (c.f., their Figure 3b). Maezawa and Hori [7] also obtain radii of 25 to 27 R_E for the distant magnetotail (-220 R_E < X_{GSE} < -150 R_E) and find the cross section of the magnetotail is cylindrical with nearly the same dimensions in the Y and Z directions under average IMF conditions. These authors find no indication of the flattening in the Z dimension reported by Sibeck et al. [8].

Bow Shock and Magnetopause
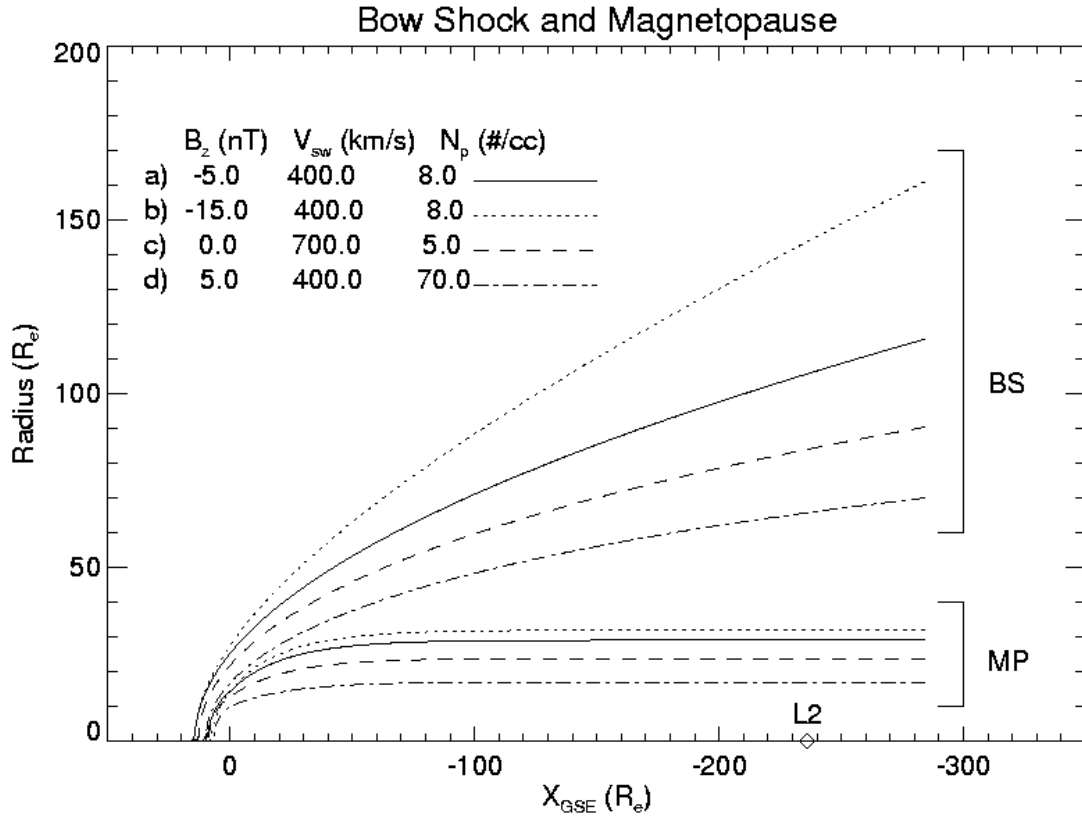
Figure 4.4 Bow Shock (BS) and Magnetopause (MP) Variability. Case (a) is typical for moderate solar wind conditions with a negative IMF B_z component. Case (b) illustrates extreme bowshock and magnetopause locations during strong $B_z < 0$ conditions. Case (c) and (d) are examples of how the boundaries respond to high speed and high density streams, respectively. The boundaries are derived from the Bennett et al. [4] and Petrinic and Russell [5,6] models. Magnetotail aberration (see section 4.2.4) is not included here.

A simple empirical relationship for the radius of the lobe based on the solar wind dynamic pressure can be obtained from the Tsyganenko [10, 11] geomagnetic field model. The radius of the lobe, R_L, and therefore of the magnetotail, is given by

$$R_L = 2.20x10^5 + 13.27 \exp(-0.366154P) \, R_E \qquad (4.1)$$

where the solar wind dyamic pressure P

$$P = nmv^2 \qquad (4.2)$$

is in units of nano-Pascals (nPa). A graphical presentation of this result is given in Figure 4.5. Equation 4.1 is used to provide a quantitative estimate of radial variations in magnetotail dimensions as a function of solar wind conditions

4.2.3 Plasma Sheet Dimensions

The dimensions of the plasma sheet are controlled by dimensions of the magnetotail which, in turn, is determined by the solar wind pressure. The Eastman et al. [9] regime identification used to characterize the Geotail data sets did not differentiate between neutral sheet and the extended plasma sheet

regions. The plasma sheet occupies a greater volume of space than the neutral sheet. Maezawa and Hori [7] obtained plasma sheet widths of 15-20 R_E based on the distributions of ion temperatures > 300 eV in the Geotail data sets. These same authors found that the plasma in the distant tail can be clearly divided into two regions by temperature: a lobe/mantle characterized by a cool dense plasma, and the plasma sheet characterized by a high temperature plasma. Similarly, statistics obtained by Christon et al. [3] suggest the plasma sheet is located within a region approximately 10 R_E in width centered in the magnetotail 68% of
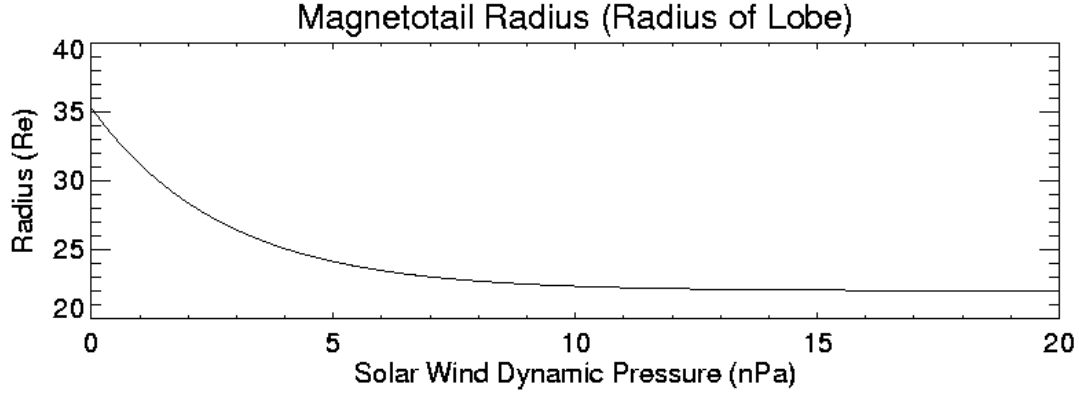
Figure 4.5 Parameterization of the Magnetotail Radius at L2 Distances. Solar wind dynamic pressure controls the radius of the magnetotail. The curve is valid over a wide range of distances about L2 since the radial dimensions of the magnetotail are nearly constant in this regime.

the time. This is based on their Figure A3c., indicating the FWHM of the plasma sheet distribution frequency is approximately 12 R_E in width. If the distribution is Gaussian, the FWHM = 2.35σ, or σ = 5.1 R_E, and 68% of the values fall within ±σ or approximately 10 R_E. Christon et al. [3] also note that while the boundary layer (or plasma mantle) and lobe exhibit a northern/southern hemisphere magnetic field polarity in the deep tail, the plasma sheet appears not to have any definite lobe structure.

In addition to variations of the plasma sheet's thickness due to changes in the solar wind dynamic pressure, the orientation of the plasma sheet also varies as a function of the time of year. This twist of the plasma sheet has been modeled in LRAD by representing the plasma sheet as comprised of two arms, each allowed to independently rotate about a hinge point. The hinge point itself is allowed to deviate from the magnetotail center.

4.2.4 Magnetotail Orientation

The orientation of the magnetotail is determined by the solar wind flow velocity. In a reference frame fixed to the rotating Sun the solar wind appears to flow radially outward into space. Figure 4.6 illustrates that in reference frames fixed to the Earth the solar wind on average appears to arrive from approximately 4 degrees east of the Sun-Earth line due to the orbital motion of the Earth through the solar wind. The aberration (or deflection) angle of the magnetotail with respect to the Sun-Earth line in the ecliptic plane is given by

$$tan\ \beta = (V_E + V_{SW,Y})\ /\ V_{SW,X} \tag{4.3}$$

where V_E is the Earth's orbital velocity. $V_{SW,X}$ and $V_{SW,Y}$ are components of the solar wind flow in the ecliptic plane parallel and perpendicular, respectively, to the Sun-Earth line. Aberration perpendicular to the ecliptic plane results if the component of the solar wind flow perpendicular to the ecliptic plane is nonzero. The angle of aberration out of the ecliptic plane is given by

$$tan\ \gamma = V_{SW,Z}\ /\ [(V_{SW,X})^2 + (V_{SW,Y})^2]^{1/2} \tag{4.4}$$
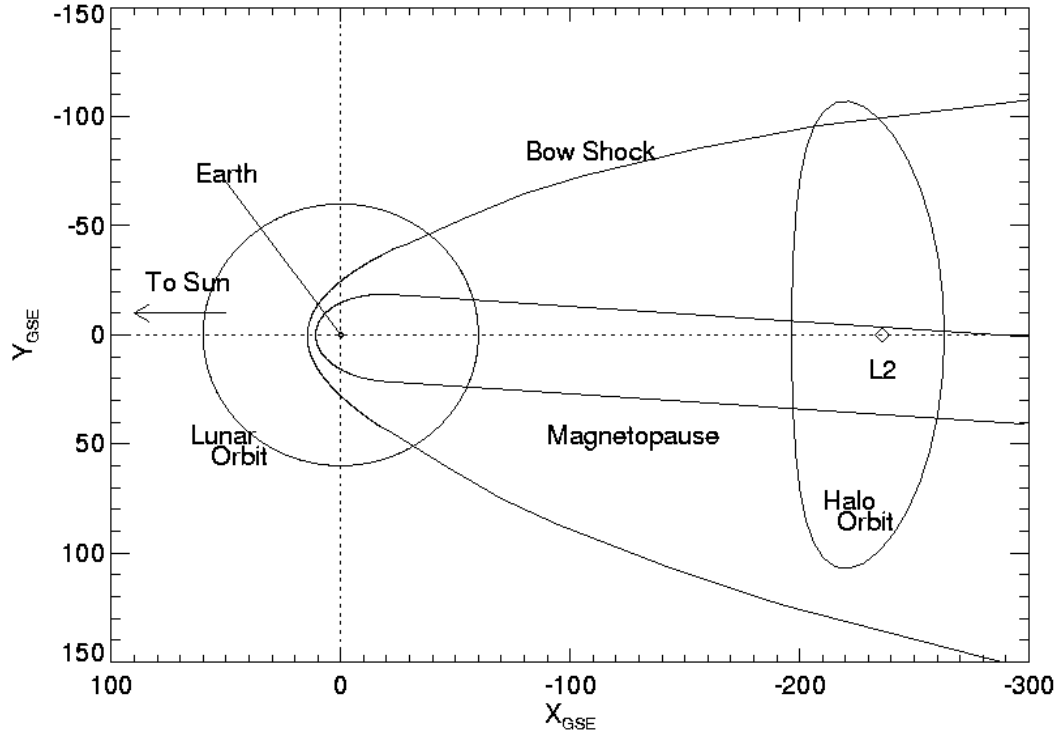
Figure 4.6 Earth-Moon System, Magnetotail, and Halo Orbit About L2. The halo orbit in this example (the same as shown in Figure 3.2) traverses all plasma regimes at L2 distances from Earth. Note the aberrated position of the magnetotail away from the Earth-Sun line due to the orbital velocity of the Earth through the solar wind.

where $V_{SW,Z}$ is the component of the solar wind flow perpendicular to the ecliptic plane. For example, an aberration angle of 4.3 degrees is obtained by adopting average values of the Earth's orbital speed, 30 km/s, and radial solar wind velocity, 400 km/s, and assuming that $V_{SW,Y} = V_{SW,Z} = 0$. The magnetotail shifts approximately 18 R_E from the Sun-Earth line at L2 under these conditions. Greater variations in orientation of the magnetotail can occur due to changes in the solar wind flow. As shown in Figure 4.7, aberration angles are variable, with the mean in the ecliptic plane near 4 degrees. At downtail distances greater than 125 R_E from the Earth, the magnetosheath is frequently observed near the X_{GSE} axis [3,6]. One cannot simply assume, therefore, that L2 is located in the magnetotail because the motion of the tail regularly moves the magnetotail far from the Sun-Earth line.

Statistics of the aberration angle are provided in Figure 4.7 where the angles are computed for the magnetotail deflections in the eclipic plane and perpendicular to the ecliptic plane. Equations 4.3 and 4.4 were used to obtain these results using the velocity components provided by the IMP-8 spacecraft over two individual one year periods. Increases in solar wind pressure (due to density or velocity enhancements) reduce the aberration angle by driving the magnetotail towards the Sun-Earth line. Large positive deflections are the result of either decreased solar wind pressure along the Sun-Earth line (decreased density or V_X velocity component) allowing the Earth's orbit motion to contribute greater weight to the numerator in Equation 4.3. In addition, increases in the solar wind V_Y component due to transient solar wind disturbances may also drive the magnetotail to large aberration angles. Large vertical aberrations require non-zero V_Z solar wind velocity components. These are most likely during transient solar wind disturbances although an average aberration of a few degrees appears to be present due to the IMP-8 bias in sampling the solar wind plasma.

20
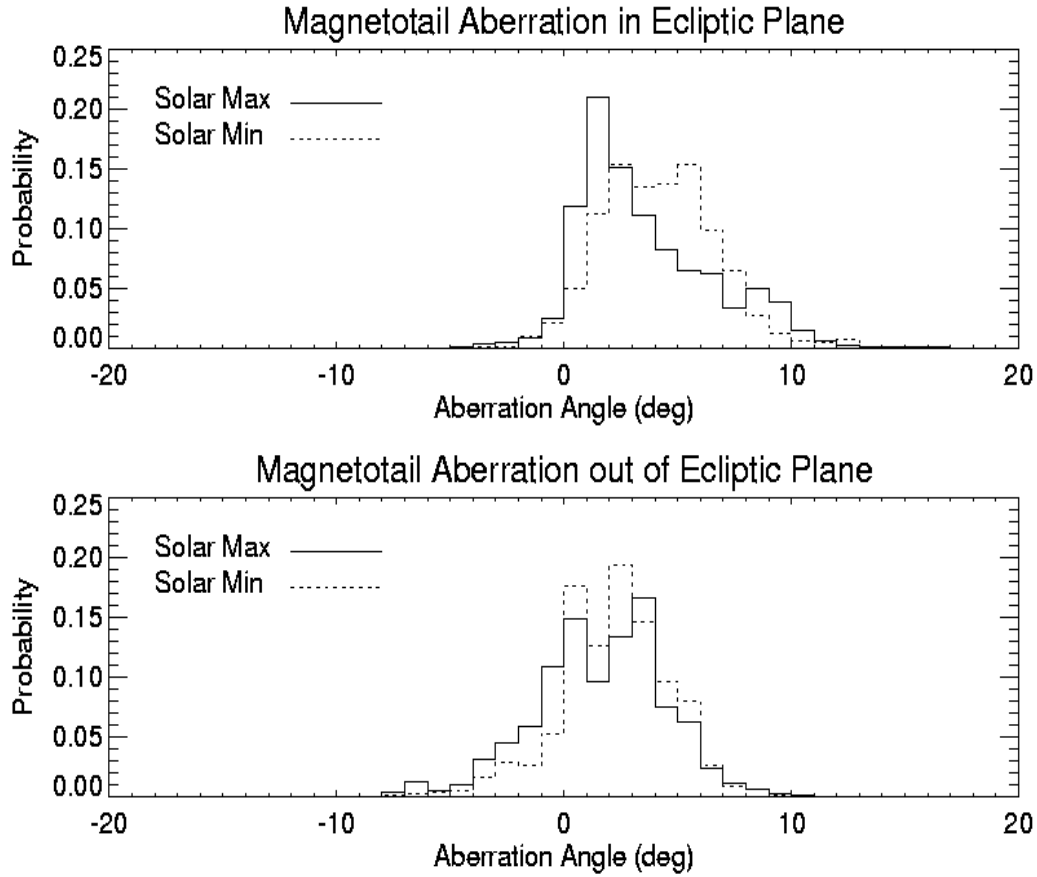
Figure 4.7 Magnetotail Aberration Angles. Variations in the ecliptic plane are generally greater than variations perpendicular to the ecliptic plane. Statistics of the aberration angles are obtained using Equations 4.3 and 4.4 with time series of IMP-8 solar wind plasma observations from 1992 (solar maximum conditions) and 1995 (solar minimum conditions).

Examples of nominal and extreme variations in the bow shock and magnetotail orientations are given in Figure 4.8. The location of L2 is indicated to illustrate that the second Lagrangian point may be located anywhere within the magnetotail or even in the magnetosheath simply due to the solar wind-dependent motion of the bow shock and magnetopause. Solar wind densities and temperatures vary on time scales of tens of minutes to days – rapid compared to the six month period of a halo orbit. Therefore, satellites in L2 halo orbits are approximately fixed in space on time scales appropriate for variations in magnetotail and magnetosheath dimension and orientation. The solar wind is the primary consideration determining the plasma regime a satellite will encounter near L2. Plasma data acquired by a satellite in the vicinity of the deep tail Sun-Earth line cannot simply be assumed to be magnetotail plasma for this reason. Similarly, NGST halo orbits will bring the satellite into contact with a variety of plasma regimes due to the combined effects of the variability in the magnetotail orientation and dimensions as well as the time varying position of the satellite along the orbit. Solar wind encounters are most likely at the furthest excursions from the Sun-Earth line when the satellite is nearest the bow shock. Magnetotail encounters will be the most likely for locations along the orbit closest to L2. In either case, the entire set of plasma regimes (solar wind, magnetosheath, and magnetotail) may be encountered depending on the solar wind conditions.

Assessment of L2 plasma conditions requires simultaneous consideration of bow shock and magnetopause boundary locations as well as the orbital motion of the spacecraft. Variability of the

magnetotail and magnetosheath on time scales (tens of minutes to days) much less than typical halo orbit periods (6 months) requires the solar wind-dependent variability to be treated for all times throughout a halo orbit. These effects are incorporated into the LRAD model to account for the range of plasma conditions that may be present along a single halo orbit. Time series of solar wind plasma conditions are used to drive the bow shock and magnetopause variations to estimate the time-dependent dimensions of the magnetotail and magnetosheath, and the solution to the halo orbit equations described in Section 3.2 is used to determine the location of the satellite.
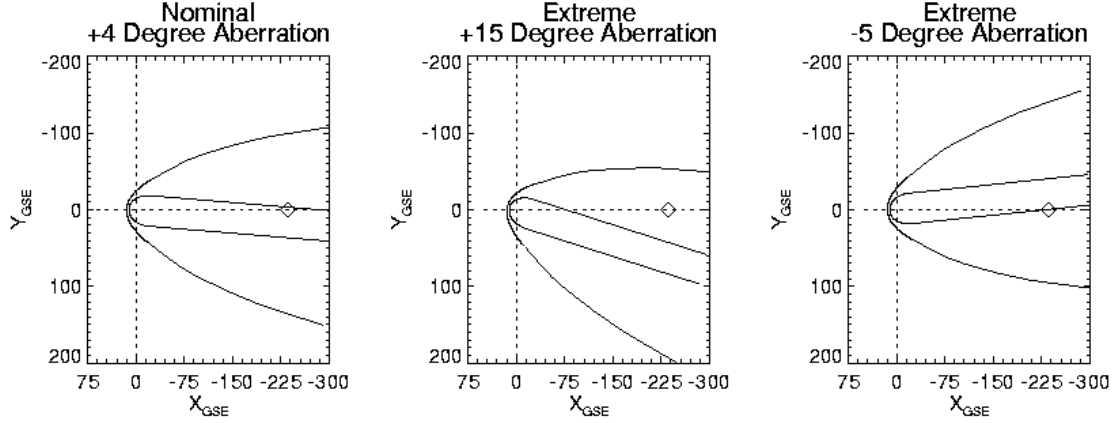
Figure 4.8 Magnetotail and Bow Shock Orientations. The nominal aberration angle of approximately 4 degrees shifts the magnetotail some 15 to 20 R_E from the Earth-Sun line at L2 distances. Large aberrations, although low probability events, move the magnetotail great distances from L2 (indicated in the figure by the diamond symbol).

Example scenes from LRAD output are provided in Figures 4.9 and 4.10 to demonstrate the variability of the plasma regimes sampled by L2 halo orbits. The first series exhibits the variations in Z-amplitude of the halo orbit for fixed dimensions of the magnetotail. There is no significant change in the Y-extent as the Z-amplitude is varied. Since the orbit's period is fixed at 180 days, once the orbit is narrow enough to intersect the magnetopause, the percentage of time the satellite spends in the plasma sheet and mantle regions is nearly constant.

(a) (b) (c)
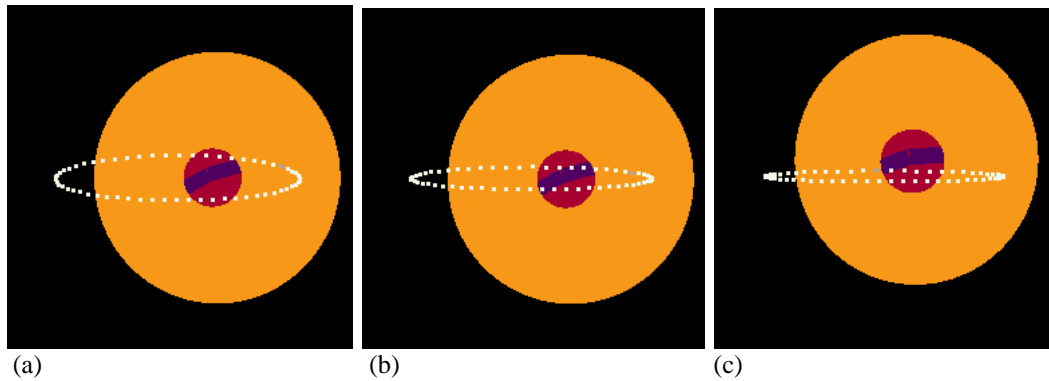
Figure 4.9 Magnetotail Cross Sections for Varying Z-Amplitude Halo Orbits. The halo orbit Z-amplitudes are (a) 125,000 km, (b) 62,000 km, and (c) 30,000 km. Each scene shows a 300 R_E by 300 R_E cross sectional area in the Y-Z plane, with trace points in the orbit marked at 3-day intervals. The magnetosheath is orange, the lobes of the magnetotail are red, the plasma sheet is blue, and the solar wind is black.

Variations in the dimensions and orientation of the tail are illustrated in the LRAD scenes in Figure 4.10. In this case a partial halo orbit is plotted in the Y-Z plane with a color-coded magnetosheath

and magnetotail in the background. Satellite locations at 3-day intervals are once again indicated along the orbit, and examples of the orbit have been randomly selected from the LRAD output. Solar wind variations drive the magnetotail to different locations as well as varying the dimensions of the magnetosheath and magnetotail. The scenes show possible configurations of the magnetotail sampled at the selected intervals due to the motion of the satellite. It is equally valid to treat each of the scenes as possible locations and dimensions of the magnetosheath and magnetotail for a single spatial location, since solar wind conditions vary on minute to hour time scales, much more rapidly than the 3-day intervals marked for each trace point.

(a)   (b)   (c)
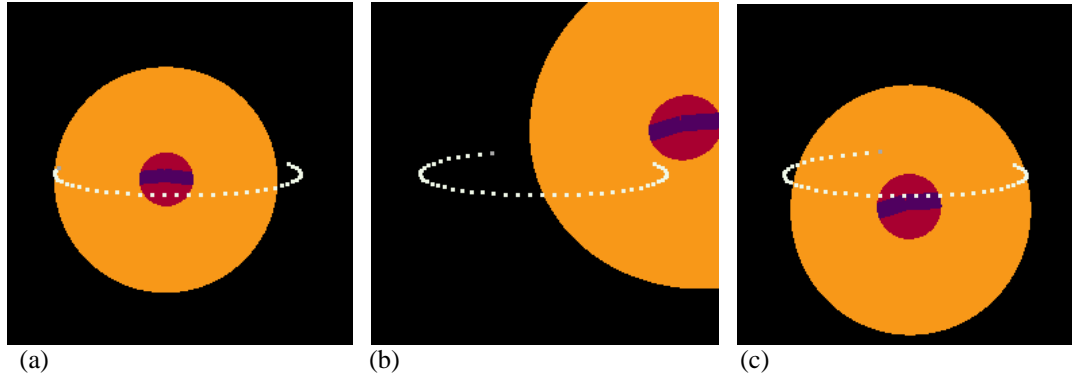
Figure 4.10 LRAD Scenes Illustrating Magnetotail Response to Solar Wind Variations. The orbit is a nominal 125,000 km Z-amplitude case in each scene with trace points plotted at 3-day intervals for selected times in the orbit. Because the dimensions and position of the magnetotail and magnetosheath may vary on time scales of minutes to hours, it is possible to encounter multiple plasma regions in very short intervals of time. The dimensions of each Y-Z cross section shown are again 300 R_E by 300 R_E. Color coding is the same in Figure 4.9.

4.3 Characteristics of Individual L2 Plasma Regimes

Information on the deep tail plasma environment (distances beyond 40 to 60 R_E from the Earth) is based almost entirely on results from two scientific satellite missions. The ISEE-3 probe crossed the magnetotail at distances of 220 to 240 R_E from the Earth in the early 1980's and provided data on the low energy plasma, energetic particles, and magnetic fields present within the magnetotail, magnetosheath, and adjacent regions in the solar wind. More recently, the Geotail spacecraft sampled the magnetotail over a range of distances to a maximum of 220 R_E from the Earth over the 2.5 year period from mid-1992 through the end of 1995. Geotail carried a comprehensive set of cold plasma, energetic particle, and magnetic and electric field sensors [12].

Statistics for plasma regimes within the magnetotail and the magnetosheath are computed from records obtained by the University of Iowa Comprehensive Plasma Instrument onboard the Geotail satellite. Plasma moments (number density, temperature, and flow velocities) from January through June 1993 are available for analysis. Four individual orbits through the deep tail are included in the data set, providing samples over a range of distances from 50 R_E downstream of the Earth to nearly 209 R_E downstream of the Earth. Although no Geotail plasma data are available from L2 itself, there is little evidence of significant variations in the number density with distance down the magnetotail in the data examined for this document. Previous studies of the magnetotail have shown that beyond approximately 50 R_E the plasma encountered in the tail is solar wind plasma that has either entered the magnetosphere through the dayside polar cusp, or locally along the open magnetopause boundary. Therefore the composition of the deep tail plasma is characteristic of the solar wind. Similar temperature characteristics are expected over a wide range of distances.

The Geotail data sets that provide the magnetotail plasma environment do not contain data on the solar wind, so an alternative source of solar wind records was required. Solar wind properties presented here are from the Interplanetary Monitoring Platform (IMP) satellites in near-circular orbits with radii from 35 to 40 R_E of the Earth. Solar wind statistics are obtained from data provided by the MIT Faraday Cup

instrument onboard IMP-8. Data from an interval starting in early November 1973 through the end of December 1998 are included, a period of time spanning almost three complete solar cycles. State-of-the-art solar wind data are now available from the WIND and ACE spacecraft, stationed about L1. However their data sets go back no further than 1995, not covering a complete solar cycle, and so have been omitted.

Although the plasma number density, temperature, and magnetic field intensity depend on the radial distance from the Sun, variations over the distance from Earth to L2 are not significant and the near-Earth plasma statistics are adopted for the L2 environment. To verify that this is a valid assumption, consider that radial variations in density scale as

$$n \propto R_S^{-2.1 \pm 0.3} \tag{4.5}$$

where R_S is the distance from the Sun to the Earth in AU [13]. Solar wind proton temperatures scale according to the relation [14]

$$T_p \propto R_S^{-0.57} \tag{4.6}$$

while electron temperatures vary according to the relation [15]

$$T_e \propto R_S^{-0.33} \tag{4.7}$$

Electron and ion temperatures in the tables in the following sections are given in multiples of 1×10^4 K to facilitate conversion to electron volts: approximate temperatures in electron volts are read directly from the tables with errors less than 20% when the conversion

$$1 \text{ eV} = 11604 \text{ K}$$

is used to convert between the units.

The average magnitude of the solar wind magnetic field is approximately 5 nT at 1 AU and varies as [14]

$$|\vec{B}| \propto 1 \Big/ \sqrt{\left(R_S^{-2} + R_S^{-4}\right)/2} \tag{4.8}$$

Adding the 0.01 AU distance from Earth to L2 to the Sun-Earth distance of 1 AU yields L2 densities, temperatures, and magnetic fields less than a few percent different from values determined in the vicinity of the Earth. Finally, no correction is required for solar wind velocity since the magnitude of the flow speed is nearly constant between 1 and 20 AU [15].

Plasma populations in all regimes at L2 are quasi-neutral, such that the electron and net ion number densities are equal. This plasma property is useful since electron densities may not be available in all plasma records. Electron densities can be estimated from the quasi-neutral condition

$$N_e = \sum_k n_k N_k \tag{4.9}$$

where n_k is the charge state of the kth ion species of density N_k in a quasi-neutral plasma. It is generally sufficient to include only hydrogen and helium ions in the sum at L2 distances, due to the relatively low abundance of heavy ions in the solar wind and distant magnetotail.

4.3.1 Solar Wind

Table 4.1 contains statistics of solar wind plasma characteristics computed using data from the IMP-6, IMP-7, and IMP-8 satellites, obtained over an interval from March 1971 through July 1974 [16].

24

These results are presented because values for the electron, proton, and helium temperatures are available in addition to the ratio of the helium to proton number densities. Plasma statistics for the same data set are divided into low- and high-speed solar wind streams in Table 4.2 to highlight the variability of solar wind parameters. Table 4.3 contains results from an extended set of IMP-8 observations from 1973 through December 1998. The latter data set, while only including proton observations, has the advantage of including nearly three complete solar cycles in the time series. It explores the range of variations in proton density, temperature, and velocity more completely than other data sets.

Table 4.1 Average Solar Wind Properties[a]

Parameter	Mean	σ	Most Probable	Median	5-95% LIMIT		
N (#/cm^3)	8.7	6.6	5.0	6.9	3.0	to	20.0
V (km/s)	468	116	375	442	320	to	710
Tp x10^4 (K)	12	9.1	5.0	9.5	0.98	to	30
Te x10^4 (K)	14	3.9	12	13	8.9	to	20
Tα x10^4 (K)	58	50	12	45	6.0	to	154
Nα/Np	0.047	0.019	0.048	0.047	0.017	to	0.078

[a]Adapted from [16].

Table 4.2 Characteristics of High and Low Speed Solar Wind[a]

Parameter	Low Speed (< 350 km/s)			High Speed (> 650 km/s)		
	Mean	σ	% Variation	Mean	σ	% Variation
N (#/cm^3)	11.9	4.5	38	3.9	0.6	15
V (km/s)	327	15	5	702	32	5
Tp x10^4 (K)	3.4	1.5	44	23	3.0	13
Te x10^4 (K)	9.3	2.1	20	10	0.98	8
Tαx10^4 (K)	7.9	5.7	68	142	30	21
Nα/Np	0.038	0.018	47	0.048	0.005	10

[a]Adapted from [16].

Table 4.3 Statistics of IMP-8 Solar Wind Proton Parameters

Cum. Prob. (%)	N (#/cm^3)	V (km/s)	T x10^4(K)	V_X (km/s)	V_Y (km/s)	V_Z (km/s)
5	2.7	317.4	3.5	-649.4	-34.0	-31.3
10	3.4	331.7	4.5	-598.7	-26.4	-20.7
33	5.4	380.3	9.0	-465.2	-13.1	2.9
50	7.2	414.6	13.5	-410.8	-4.5	17.2
67	9.8	469.4	20.5	-376.6	5.9	26.1
90	18.4	603.5	42.4	-328.0	31.9	46.6
99	39.5	742.4	101.4	-290.4	78.1	85.7

Solar wind electrons are composed of two populations: a low-energy component which dominates the assemblage, and a high-energy component with ten times the temperature, but with only one tenth the number density [15]. A bi-Maxwellian distribution is required to fit the statistics of these mixed components. Unfortunately, the two-component plasma moments from this distribution are not generally available. The solar wind statistics presented here therefore pertain primarily to the dominant core population.

Table 4.4 gives the species composition in the average solar wind for a variety of solar wind conditions. Examples for average solar wind, low speed solar wind, high speed solar wind, and a coronal mass ejection driver gas are given to demonstrate the variability of ion composition for different solar wind conditions. Hydrogen ions dominate in all cases, with helium the most common minor species. Ions heavier than helium are present in the solar wind but represent a negligible contribution to the total solar wind mass. This same relative composition also applies throughout the magnetosheath and into the magnetotail at L2 distances, because the plasma source for the magnetotail beyond approximately 100 R_E from the Earth is primarily the solar wind [18].

Table 4.4 Solar Wind Composition

	Relative Abundance			
Element	Average[a]	Low Speed[b]	High Speed[b]	CME Driver Plasma[b]
H	1.0	1.0	1.0	1.0
^{3}He	1.7×10^{-5}			
^{4}He	4.0×10^{-2}			
He	4.0×10^{-2}	0.04	0.04	>.15
O	5.2×10^{-4}	5.0×10^{-4}	8.0×10^{-4}	7.5×10^{-4}
^{20}Ne	7.0×10^{-5}			
^{21}Ne	1.7×10^{-7}			
^{22}Ne	5.1×10^{-6}			
Ne	7.5×10^{-5}	8.5×10^{-5}	---	---
Si	7.5×10^{-5}			
Ar	3.0×10^{-6}			
Fe	5.3×10^{-5}	5.0×10^{-5}	---	9.1×10^{-5}

[a]Adapted from [16].
[b]Adapted from [17].

Tables 4.1, 4.2, and 4.3 provide the necessary information required for input into a spacecraft charging analysis. It should be noted that use of these values is complicated by the requirement that correlations between the individual values must be considered to obtain meaningful results for extreme values of the electron and proton flux. For example, solar wind densities and speeds are generally anti-correlated, with the greatest densities occurring during periods of low speed flows and the smaller densities occurring in high speed flows. This inverse relationship is given by the equation

$$N = C \, V^{-3/2} \tag{4.10}$$

where C is a constant of proportionality [19]. The solar wind velocity and temperature, however, are correlated:

$$T^{1/2} = A \, V + B \tag{4.11}$$

where the temperature is in units of 1000K and the velocity is in km/s [19]. The parameters

$$A = 0.033 \pm 0.0001, \qquad B = -4.8 \pm 0.4$$

have been found to be relatively constant for solar wind measurements taken over the period from 1966 through 1971, a significant fraction of a solar cycle [20].

4.3.2 Magnetosheath

Magnetosheath plasma characteristics given in Table 4.5 are obtained from the Geotail deep tail (<220 R_E) observations. Note that while the magnetosheath flow is variable, it is always in the anti-solar direction, consistent with the solar wind flow. Plasma parameters not included in the table scale with the solar wind values:

$$T_{alpha} = T_{proton} \; , \;\; N_{alpha}/N_{proton} = 0.047 \; , \;\; N_e \text{ from quasineutrality (Eq. 4.9)}.$$

Table 4.5 Statistical Variations in Magnetosheath Parameters

Magnetosheath Parameters[a]

Cumulative Prob.	N_i (#/cc)	T_i x10^4 (K)	T_e x10^4 (K)	V_X (km/s)	V_Y (km/s)	V_Z (km/s)
5	0.283	18.6	3.12	-519	-93.6	-52.3
10	0.362	37.1	6.24	-493	-76.4	-39.0
33	0.687	75.5	20.6	-383	-50.0	-15.8
50	1.006	92.7	31.2	-311	-32.9	- 7.21
67	1.645	110.	41.8	-272	-12.1	- 0.88
90	6.082	215.	56.2	-193	28.2	9.14
99	8.684	461.	111.	-112	75.1	35.3

[a]Based on analysis of Geotail Comprehensive Plasma Instrument records.

4.3.3 Boundary Layer

The boundary layer at L2 distances is solar wind plasma that crossed the locally open magnetopause. This plasma drifts slowly towards the magnetosheath as it continues to move antisunward at near solar wind speeds. Parameters for the magnetotail boundary layer are given in Table 4.6 Electron and helium plasma characteristics not available in the magnetotail lobe parameter table scale with the solar wind values of the boundary layer plasma, as in the case above for the magnetosheath.

Table 4.6 Statistical Variations in Boundary Layer Parameters

Boundary Layer Parameters[a]

Cumulative Prob.	N_i (#/cc)	T_i x10^4 (K)	T_e x10^4 (K)	V_X (km/s)	V_Y (km/s)	V_Z (km/s)
5	0.108	30.9	6.03	-297.	-61.2	-68.8
10	0.131	58.9	12.1	-264.	-47.0	-52.7
33	0.235	90.3	39.8	-199.	-18.8	-23.6
50	0.316	114.	60.7	-167.	-5.67	-12.0
67	0.440	165.	84.9	-139.	6.87	- 1.90
90	0.867	363.	124.	-70.2	32.8	18.1
99	2.286	1220.	272.	2.49	74.4	58.7

[a]Based on analysis of Geotail Comprehensive Plasma Instrument records.

4.3.4 Magnetotail Lobe

The composition of the distant magnetotail is similar to the solar wind; variations in the individual parameters are given in Table 4.7. Electron and helium plasma characteristics not available in the magnetotail lobe parameter table scale with the solar wind values, as before.

Table 4.7 Statistical Variations in Magnetotail Lobe Plasma Parameters[a]

Cumulative Prob.	N_i (#/cc)	T_i $\times 10^4$ (K)	T_e $\times 10^4$ (K)	V_X (km/s)	V_Y (km/s)	V_Z (km/s)
5	0.010	93.7	75.2	-194.	-119.	-202.
10	0.021	129.	92.4	-121.	- 82.3	-153.
33	0.069	405.	151.	-50.5	- 23.0	- 79.3
50	0.107	627.	205.	-24.0	5.62	- 55.4
67	0.166	1180.	303.	11.5	33.6	- 28.5
90	0.345	2730.	487.	153.	79.0	15.0
99	0.620	5880.	1650.	330.	208.	124.

[a]Based on analysis of records from the Comprehensive Plasma Instrument on the Geotail satellite.

4.3.5 Plasma Sheet

Plasma in the distant magnetotail's plasma sheet is primarily solar wind that has crossed the open magnetopause and drifted towards the neutral sheet. The plasma sheet particle density is a maximum at the center (at the neutral sheet), and is modeled as linearly decreasing with distance from the neutral sheet to the particle density seen at the plasma sheet boundary layer. The ion temperature is also maximum at the neutral sheet and falls off in a linear fashion to the temperature seen at the edge of the plasma sheet boundary layer. The bulk flow speed, however, is a minimum at the neutral sheet and increases towards the plasma sheet boundary layer. Electron and helium characteristics not given in Table 4.8 scale as:

Number density at neutral sheet :   1.0 cm^{-3}
Number density at plasma sheet boundary layer :   0.1 cm^{-3}
Neutral sheet electron temperature: 8.0 x 10^7 K
Plasma sheet boundary layer electron temp.:   1.2 x 10^6 K
Proton temperature, $T_p = 5.5\ T_e$
Helium temperature, $T_{alpha} = T_p$
N_e is obtain from the quasi-neutrality condition
$N_{alpha}/N_{proton} = 0.047$

Table 4.8 Statistical Variations in Plasma Sheet Properties[a]

Cumulative Prob.	N_i (#/cc)	T_i $\times 10^4$ (K)	T_e $\times 10^4$ (K)	V_X (km/s)	V_Y (km/s)	V_Z (km/s)
5	0.015	185.	60.0	-378.	-104.	-148.
10	0.029	246.	72.8	-308.	- 75.0	-115.
33	0.096	472.	130.	-134.	- 25.4	- 58.0
50	0.146	708.	169.	- 62.0	- 4.87	- 36.0
67	0.196	1100.	228.	- 10.1	14.7	- 17.4
90	0.395	2260.	419.	87.6	60.0	17.2
99	1.361	4740.	753.	308.	154.	81.0

Plasma Sheet Parameters[a]

[a]Based on analysis of Geotail Comprehensive Plasma Instrument records.

4.4 Electron, Proton, and Helium Flux Calculations

Flux estimates are obtained in the LRAD model using a drifting Maxwellian velocity distribution of the form [21]:

$$f_i(\mathbf{r}, \mathbf{v}) = n_i \left(\frac{m_i}{2\pi k T_i} \right)^{3/2} \exp\left[-\frac{m_i(\mathbf{v} - \mathbf{u})^2}{2k T_i} \right] \tag{4.12}$$

where $\mathbf{r}$ is particle position, $\mathbf{v}$ is particle velocity, $\mathbf{u}$ is the solar wind bulk velocity, and the ith species (i = electron, hydrogen ion, helium ion, etc.) is characterized by the number density n_i, mass m_i, and temperature T_i. The directional flux of the ith species is given by the first order velocity moment:

$$flux_i = \int \mathbf{v} \ f_i(r, \mathbf{v}) d^3\mathbf{v} \tag{4.13}$$

Fluxes are computed using the LRAD plasma environment model. Computation of mean and limiting values of the particle flux and fluence requires a more sophisticated analysis than that required for estimating the statistics of the individual plasma parameters. Although it is tempting to simply insert the appropriate statistical values of the plasma characteristics provided in previous sections into equation 4.12, correlations between plasma density, velocity, and temperature values must be maintained since they are used simultaneously to determine particle flux and fluence. A further complication arises because the fluctuating conditions in the solar wind determine the variable dimensions of the magnetotail and magnetosheath as well as changes in the orientation of the magnetotail. Particle flux and fluence estimates must consider this variability because the rapid motion of the magnetosphere and magnetosheath boundaries may, for example, place the satellite within the magnetotail at one point in time and in the magnetosheath only a few minutes later, even though the satellite has moved only a small distance in its orbit. The combined effects of the orbital geometry and variability of the magnetopause and bow shock locations determine the environment sampled by a satellite in an L2 halo orbit at any given time. Proper assessment of the environment's impact on a satellite at L2 requires consideration of these combined effects.

Two assumptions are implicit in using equations 4.12 and 4.13 to compute particle fluxes. First, equation 4.12 applies only for non-relativistic particles. This assumption is certainly valid for all plasma ions under consideration here, since the maximum energy considered (100 keV) is a small fraction of the 938 MeV proton rest mass. Although electrons of 100 kev have energies approaching twenty percent of their 511 keV rest mass, electron energies near the peak of the electron fluxes are less than 1 kev for all L2 plasma regimes. Second, the number densities, velocities, and temperatures from the IMP-8 and Geotail data are obtained by performing a numerical integration of the velocity moments

$$< v_i^n > = \sum_{k=0}^{max} v_k^n f_i(v_k) \Delta v \tag{4.14}$$

where the distribution function $f_i(v_k)$ is the velocity distribution function for the ith species obtained by the instrument at a discrete set of v_k velocities. The observed distribution function need not necessarily be a Maxwellian to implement this algorithm. The number density, flux, velocity, and temperature are then obtained by computing the appropriate moment, n = 0,1,2,…, of the velocity distribution (c.f., Purvis et al., [21]). Since the original velocity distribution functions are not available for analysis, we are forced to assume that all the distribution functions are Maxwellian. This assumption is not expected to create significant errors since in general the low energy plasma populations in the solar wind, magnetosheath, and magnetotail are represented sufficiently well by Maxwellians that this technique is reasonable for the problem at hand [22,23].

Statistics for the electron, proton, and helium fluxes are obtained using the following process: within each of the regions for which plasma data is available, including the solar wind, magnetosheath, plasma mantle, and plasma sheet, a series of fluxes is computed for each data value. The correlations

29

between density, velocity, and temperature are maintained by using the moments in Eq. 4.12 to compute the flux with Eq. 4.13. A differential flux spectrum is computed for each record in the data files, and the resulting flux binned according to energy. Finally, the statistics of the flux within an individual energy bin are computed. The final plots and tables provided for flux are therefore statistical flux values within individual energy ranges and should not be confused with energy spectra. Statistical results are obtained in this way for fluxes in the solar wind, magnetosheath, plasma mantle, and plasma sheet. Lobe and plasma mantle environments are combined into a single plasma mantle in the LRAD model, since very few lobe identifications were present in the Geotail data. The energy bins selected range from 1 eV to 100 keV, providing adequate coverage to allow examination of material surface and thin film effects, as well as spacecraft surface charging.

The bulk flow of the solar wind is evident in Figure 4.11 as the peaks in the statistical ion fluxes. Protons exhibit a peak in the statistical flux near 1 keV which is consistent with an average solar wind velocity on the order of 400-500 km/sec. The peak in the statistical helium flux is approximately 4 keV because the alpha particle is four times as massive as the proton but moves at the same bulk flow velocity.
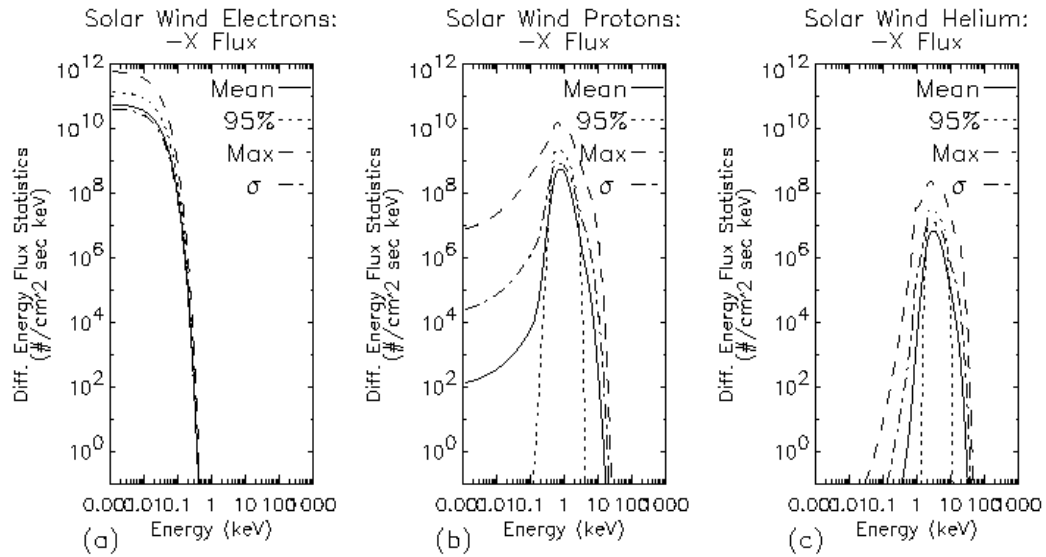

Figure 4.11 Solar Wind Flux Statistics. Both proton and helium fluxes are dominated by the bulk motion of the ions while the electron flux is dominated by the thermal motion of the plasma.

Thermal motions in the ion populations are evident from the width of the the flux peaks. In contrast, the bulk flow speed of the solar wind provides electrons with energies of only a fraction of an electron volt. Electrons are dominated by their thermal motion and no obvious peak is present in the statistical fluxes.

Magnetosheath statistical fluxes are shown in Figure 4.12. Conversion of the bulk flow energy into thermal motion of the plasma is evident in the ion fluxes by the enhanced fluxes at energies less than a few keV. Under average conditions, the value of the solar wind proton flux is approximately 10^8 to 10^9 protons/cm^2-sec-keV at energies near 1 keV. This value is reduced by about a factor of 10 in the magnetosheath at 1 keV. Note however that for energies of 0.1 keV, one tenth the bulk flow energy, proton fluxes are enhanced in the magnetosheath by over three orders of magnitude. There appear to be two populations of electrons in the magnetosheath statistical flux plot. However, this characteristic is probably due to undersampling the deep tail plasma populations.

Ion fluxes within the magnetotail are found to be reduced in intensity compared to the magnetosheath and solar wind. Peak fluxes under average conditions in the plasma mantle and plasma sheet shown in Figures 4.13 and 4.14 are less than 10^7 protons/cm^2-sec-keV. Corresponding values for the

magnetosheath are between 10^7 and 10^8 protons/cm²-sec-keV while in the solar wind the peak fluxes are on the order of 10^8 to 10^9 protons/cm²-sec-keV.
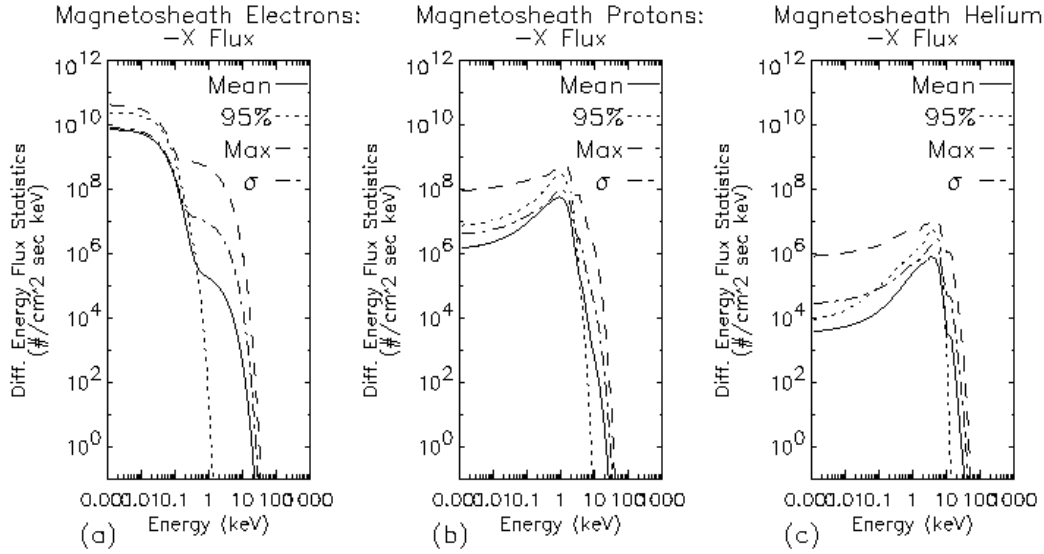

Figure 4.12 Magnetosheath Flux Statistics.   Thermalization of the ion flow is evident by the increase in flux at energies less than the peak in the statistical flux.
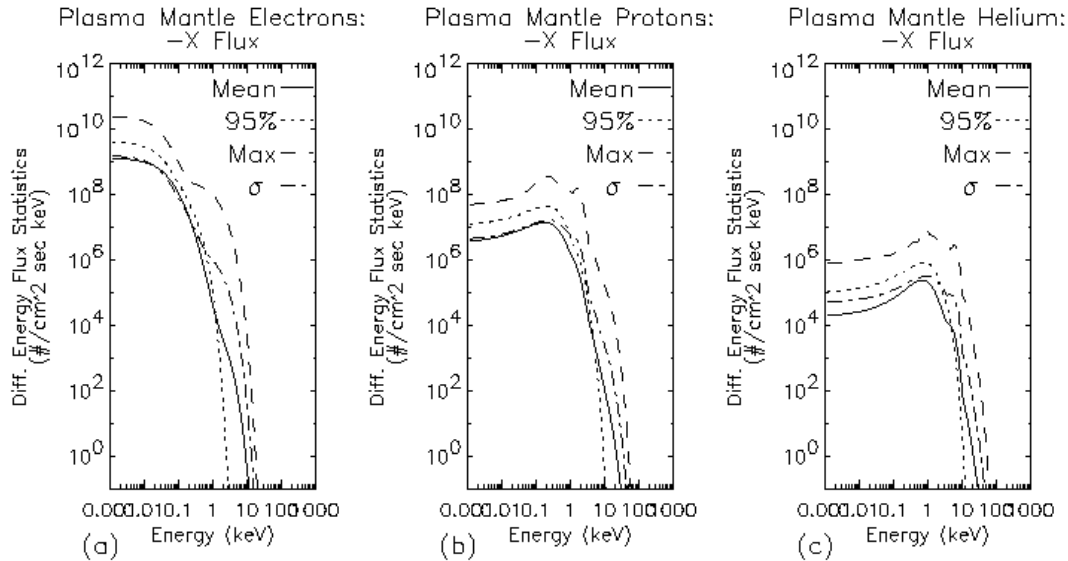

Figure 4.13 Plasma Mantle Flux Statistics.   Plasma mantle ion fluxes are similar to the magnetosheath because the predominant source of plasma in the deep tail is the magnetosheath.
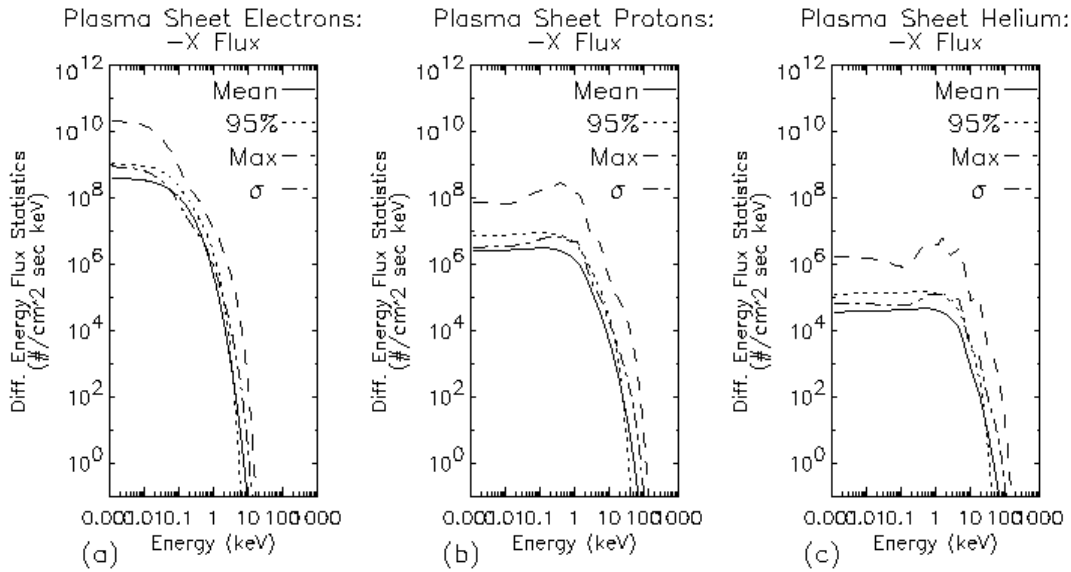
31

Figure 4.14 Plasma Sheet Flux Statistics.

4.5 Electron, Proton, and Helium Fluence Calculations

In order to give total dosage estimates, it is necessary to calculate the time integral of the flux, or fluence. As noted in Section 3.2, the typical value for a halo orbit period is approximately 180 days. In fact, a characteristic of L2 halo orbits is that their periods are always close to 180 days, regardless of the orbit amplitude. Fluence calculations are therefore provided for a period of 180 days (6 months) to sample a complete orbit. Results are obtained for a number of halo orbit amplitudes to highlight fluence variations that may exist for different orbital conditions. A halo orbit model employing the equations and parameter values of Richardson [24, 25] is included in LRAD to provide the orbital ephemeris required for the fluence calculation. The accumulated electron or ion fluence over a given orbit depends on a number of factors. The variability of the plasma sampled by the spacecraft over the orbit must be considered, since the spacecraft will encounter varying plasma populations even if it resides in a single plasma regime. Orientation of the magnetosphere due to solar wind velocity variations and the variability in the bow shock and magnetopause locations due to solar wind density and temperature variations must also be considered. To obtain the statistical fluences, these effects are included in LRAD as follows:

1) The halo orbit equations are used to determine the position of the spacecraft as a function of time.
2) At each increment in time along the halo orbit, a set of 1000 solar wind conditions is drawn randomly from a one year time series of IMP-8 solar wind records.
3) For each of the solar wind conditions, the orientation and dimensions of the magnetotail and magnetosheath are determined, and the plasma regime in which the satellite resides is identified.
4) A series of (typically on the order of 1000) random draws on the plasma records is used to sample the range of plasma conditions present within the identified plasma regime.
5) A flux is derived from each set of plasma records. Summing the fluxes along the orbit yields a fluence.
6) Statistical fluences are obtained by binning the fluxes for each of the time steps along the orbit.

32

Only representative examples are provided here for directional differential fluences along the direction of maximum flux, $-X_{GSE}$ in all cases. Complete sets of plots and tabular data for the statistical differential fluence for each direction are presented in Appendix B of the Addendum.
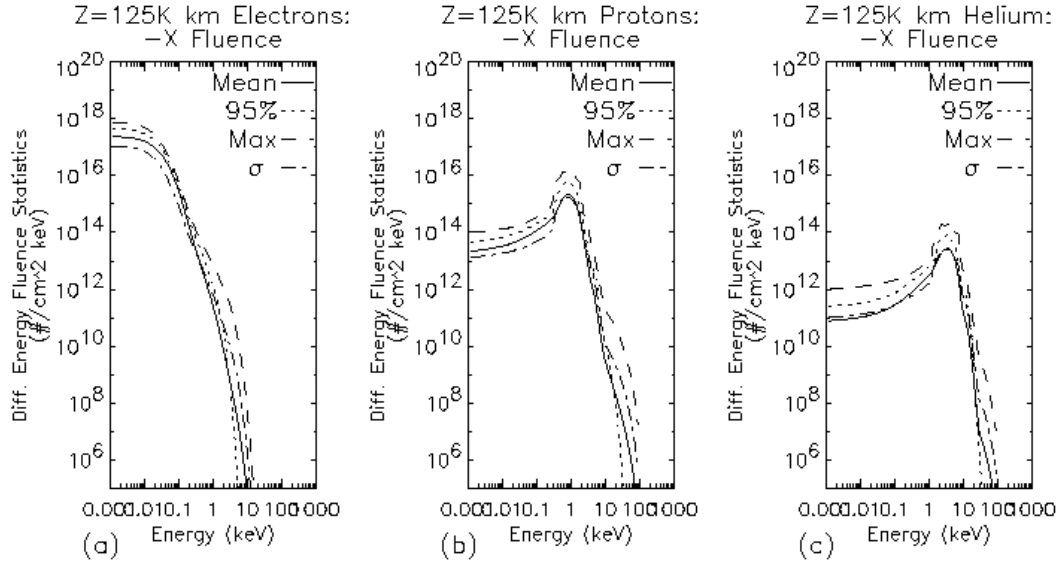

Figure 4.15 Fluence for a Single 125,000 km Z-Amplitude Halo Orbit. Solar wind values from 1992 were used to drive the magnetosheath and magnetotail variations.

Table 4.9 125,000 km Z-Amplitude Halo Orbit Satellite Location Summary

Number of Monte Carlo Runs	:	1000
Total duration of problem	:	180.0000 days
Inside Solar Wind Region	:	12.77 % of the time (22.99 days)
Inside N/S Lobe Region	:	0.00 % of the time (0.00 days)
Inside Plasma Sheet Region	:	3.22 % of the time (5.80 days)
Inside Plasma Mantle Region	:	5.91 % of the time (10.63 days)
Inside Magnetosheath Region	:	78.11 % of the time

Statistical fluences illustrated in Figure 4.15 are derived for the 125,000 km Z-amplitude halo orbit shown in Figure 3.2. Solar wind data from 1992 were used to obtain the magnetopause and bow shock variations, yielding results appropriate for solar maximum conditions. Ion fluences are dominated by the bulk flow, as shown by the peak in the fluences at energies near the peak fluxes. For comparison, Figure 4.16 provides a similar set of fluences for the 30,000 km Z-amplitude halo orbit. There is relatively little difference between the results for the large amplitude orbit and the small amplitude orbit. Although there is a difference of 95,000 km between the Z-amplitudes of the two orbits, this difference is less than the diameter of the magnetotail. The rate at which the satellite samples the magnetosheath and the magnetotail primarily depends on the solar wind variations, not the orbit parameters. A summary of the statistics of the fluence calculation is given in Table 4.9, showing the percentage of time the satellite spends in each plasma regime during a single pass through the 125,000 km Z-amplitude orbit. Table 4.10 shows the same results for the 30,000 km Z-amplitude orbit. Differences between the two cases are not significant.

Table 4.10 30,000 km Z-Amplitude Halo Orbit Satellite Location Summary

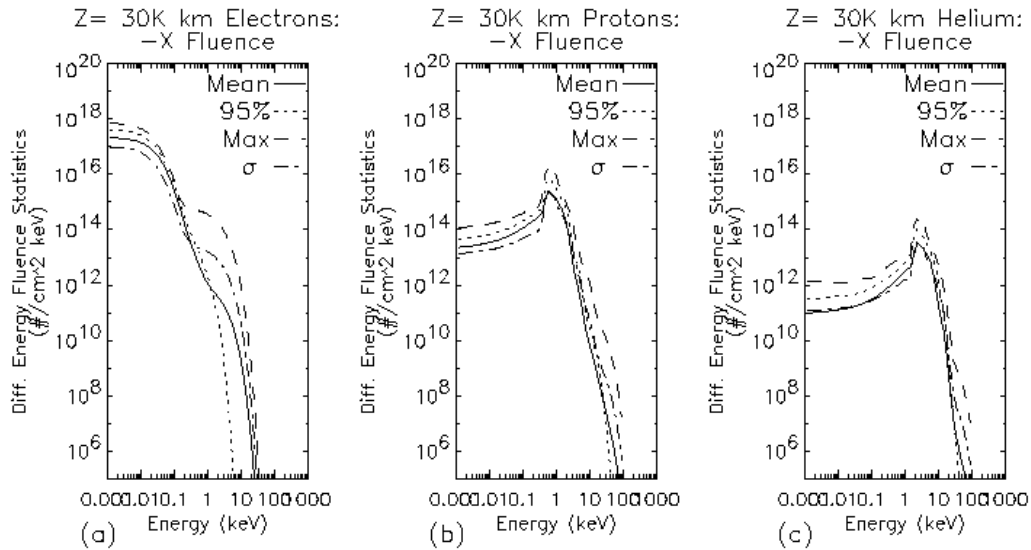|		
Number of Monte Carlo Runs	:	1000
Total duration of problem	:	180.0000 days
Inside Solar Wind Region	:	12.51 % of the time (22.52 days)
Inside N/S Lobe Region	:	0.00 % of the time (0.00 days)
Inside Plasma Sheet Region	:	4.81 % of the time (8.65 days)
Inside Plasma Mantle Region	:	9.39 % of the time (16.89 days)
Inside Magnetosheath Region	:	73.30 % of the time (131.94 days)

Figure 4.16 Fluence for a single 30,000 km Z-amplitude halo orbit. Solar wind values
from 1992 were used to drive the magnetosheath and magnetotail variations.

4.6 Other Issues

The previous sections described the conditions in the ambient low energy plasma environment. During periods of enhanced geomagnetic activity, substorms may produce additional fluxes of energetic plasma particles that may be of concern, in addition to a low density, high energy background particle population present in the magnetotail that is not included in the current LRAD model. The two primary species of concern are ions of sufficient energy to contribute to enhanced material degradation, and relativistic electrons, which may contribute to bulk dielectric charging. In addition to these, energetic protons released during solar eruptive events will be present from time to time, their prevalence linked to the stage of the solar activity cycle. These particles are discussed in greater detail in Chapter V.

4.6.1 Relativistic Electrons

Richardson et al. [26] show observations of 0.2-2.0 MeV electrons with average fluxes of approximately 10^{-2} electrons/cm^2-sec-sr-MeV and periodic enhancements, or bursts, 2 to 10 times greater than the background. Ion measurements obtained at the same time at 1-4 MeV/amu do not exhibit the enhancements; the ion flux levels are the same as those of the 1.15-1.40 MeV protons reported by IMP-8, demonstrating that the ion component in the magnetotail is dominated by the ambient solar background particles. Durations of the electron bursts are typically less than an hour (97% identified in the ISEE-3 data had durations less than 1 hour, 47% of the bursts were less than 15 minutes). Richardson et al. summarize their findings as follows:

34

1) Approximately 60% of bursts are found in the plasma sheet, and approximately 40% are seen in the lobe, although they are observed in all tail regions.
2) The intensity and occurrence rate both decrease abruptly by a factor of 10 at distances of 80 to 90 R_E down the magnetotail.
3) Although statistics are poor in the deep tail (beyond 100 R_E), event rates in the plasma sheet are approximately 0.6 events/hr at distances of 0 to 100 R_E, and 0.1 to 0.6 events/hr from 100 to 250 R_E. At L2, the rate is approximately 0.2 events/hr. Rates in the lobe are <0.1 events/hr for distances greater than 100 R_E down the tail.
4) Intensities of 0.2 – 2.0 MeV electron bursts observed between 200 to 240 R_E vary from 0.02 to 0.10 electrons/cm^2-s-sr-MeV in both the plasma sheet and the lobe.

The significance of the relativistic electron events to spacecraft at L2 will depend on the rate at which charge is deposited in dielectric materials compared to the rate at which it can be dissipated. A critical parameter is the dielectric conductivity since rapid redistribution of the electrons deposited in materials during an event will minimize the charge accumulation in localized regions and reduce the possibility of breakdown of the dielectric through an electric discharge.

A simple order of magnitude estimate for the importance of the events is provided by comparing the electron fluence in a single event to the critical fluence of 5×10^{11} electrons/cm^2 obtained by Hastings and Garrett [27] for the dielectric breakdown of a parallel plate capacitor. Consider an hour interval for which the electron flux of 0.2-2.0 MeV electrons is 1×10^{-1} electrons/cm^2-sec-sr-MeV. The electron fluence for this event is on the order of 9×10^3 electrons/cm^2, much less than the critical fluence reported by Hastings and Garrett. The relatively low rate of the events further suggests that the spacecraft is unlikely to encounter intervals where multiple events lead to enhanced electron fluxes.

It is instructive to compare the deep tail electron bursts with an additional energetic electron source for bulk dielectric charging: solar energetic particles. Fluxes of 0.2-2.0 MeV electrons generated during coronal mass ejections may exceed 1×10^1 electrons/cm^2-sec-sr-MeV for of intervals of three hours or more and 1×10^{-1} electrons/cm^2-sec-sr-MeV for periods of 24 to 48 hours or more [28]. The electron fluence in these events are on the order of 3×10^6 electrons/cm^2 for the three hour intervals and may exceed 4×10^7 electrons/cm^2 for events where the elevated flux of energetic particles persist for 48 hours or longer.

A complete assessment of the impact of energetic electrons on the NGST spacecraft, whether solar or terrestrial in origin, will require detailed information on the materials and construction techniques for the spacecraft. It is also recommended that if materials with low conductivity and small thresholds for dielectric breakdown are chosen, particularly for critical structures or systems, then a more detailed examination of the energetic electron environment may be warranted.

4.6.2 Energetic Ionospheric Ions Associated with Substorms

Observations of episodic enhancements of energetic ions have also been reported from the deep magnetotail. Gloeckler et al. [29] report ISEE-3 observations of protons, helium, and heavy ions. The presence of significant numbers of heavy ions (beyond those typically observed in the solar wind) suggests a source in the near-Earth magnetosphere and ionosphere. Christon et al. [30] report Geotail/EPIC observations of atomic and molecular ions at $X_{GSE} = -146$ R_E associated with substorms. The reported composition of the plasma is primarily protons (approximately 90%), with a variety of minor species. Abundances of the individual species relative to protons are given in Table 4.11. In any event, we note that observations of storms and substorms in this region are limited, and the full storm impact may not be well known.

Table 4.11 Ion Composition of Deep Tail Energetic Ion Enhancements (from [30]).

Species	Abundance Relative to protons
H+	1.0
He+	0.0024 - 0.0048
He+2	0.02 - 0.04
O+	0.02 - 0.04
CNO+3	0.0004 - 0.0016
N+	0.005 - 0.0036
O_2+	0.0002 - 0.0008
NO+	0.0002 - 0.0008
N_2+	0.0002 - 0.0008

4.7 Summary

A spacecraft in a L2 halo orbit can expect to encounter all regions of the magnetotail, as well as the free solar wind. This is due to variations in the magnetotail size and direction, which are determined by fluctuations of the solar wind speed, direction, pressure, and density. During its immersion in the magnetotail, the spacecraft will be afforded some protection from energetic particles emitted by the Sun, e.g., by solar proton events, but it may be subjected to bombardment by energetic particles such as heavy ions and relativistic electrons during magnetospheric storms and substorms.

With certain exceptions noted above, the energies of the particles found in the plasma regimes discussed in this chapter are insufficient to penetrate spacecraft shielding; a discussion of energetic, penetrating particles is found in the next chapter. The principal impact of the solar wind and magnetospheric plasmas on spacecraft will be degradation of surfaces and the accumulation of charge. Designers of spacecraft instruments, electrical systems, optical surfaces, insulation and shielding, and structures must take these charging and surface effects into account in their design processes.

4.8 Acknowledgements

References

[1] Brace, L. H., "Langmuir Probe Measurements in the Ionosphere," in *Measurement Techniques in Space Plasmas: Particles,* Geophysical Monograph 102, edited by R.B. Pfaff, J.E. Borovsky, and D.T. Young, pp. 23 – 35, American Geophysical Union, Washington, D.C., 1998.

[2] Rosenbauer, H., H. Grunwaldt, M. D. Montgomery, G. Paschmann, and N. Sckopke, "HEOS-2 Plasma Observations in the Distant Polar Magnetosphere: The Plasma Mantle," J. Geophys. Res., **80**, 2723, 1975.

[3] Christon, S.P., T.E. Eastman, T. Doke, L.A. Frank, G. Gloeckler, H. Kojima, S. Kokubun, A.T.Y. Lui, H. Matsumoto, R.W. McEntire, T. Mukai, S.R. Nylund, W.R. Paterson, E.C. Roelof, Y. Saito, T. Sotirelis, K. Tsuruda, D.J. Williams, and T. Yamamoto, "Magnetospheric Plasma Regimes Identified Using Geotail Measurements 2. Statistics, Spatial Distribution, and Geomagnetic Dependence,"J. Geophys. Res., **103**, 23521 – 23542, 1998.

[4] Bennett, L., M. G. Kivelson, K. K. Khurana, L. A. Frank, and W. R. Paterson, "A Model of the Earth's Distant Bow Shock," J. Geophys. Res., **102**, 26927 – 26941, 1997.

[5a] Petrinec, S. M. and C. T. Russell, "An Empirical Model of the Size and Shape of the near-Earth Magnetopause," Geophys. Res. Lett., **20**, 2695 - 2698, 1993.

[5b] Petrinec, S. M. and C. T. Russell, "Factors Controlling the Shape and Size of the Post-Terminator Magnetopause," Advances in Space Research, **18**, (8)213-(8)216, 1996.

[6] Fairfield, D. H., "On the Structure of the Distant Magnetotail: ISEE-3," J. Geophys. Res., **97**, 1403-1410, 1992.

[7] Maezawa, K., and T. Hori, "The Distant Magnetotail: Its Structure, IMF Dependence, and Thermal Properties," in *New Perspectives on the Earth's Magnetotail,* AGU Monograph 105, (ed. by A. Nishida, D. N. Baker, and S. W. H. Cowley), American Geophysical Union, Washington, D.C., pp. 1 – 19, 1998.

[8] Sibeck, D. G., G. L. Siscoe, J. A. Slavin, and R. P. Lepping, "Major Flattening of the Distant Geomagnetic Tail," J. Geophys. Res., **91**, 4223, 1986.

[9] Eastman, T.E., Christon, S.P., T. Doke, L.A. Frank, G. Gloeckler, H. Kojima, S. Kokubun, A.T.Y. Lui, H. Matsumoto, R.W. McEntire, T. Mukai, S.R. Nylund, W.R. Paterson, E.C. Roelof, Y. Saito, T. Sotirelis, K. Tsuruda, D.J. Williams, and T. Yamamoto, "Magnetospheric Plasma Regimes Identified Using Geotail Measurements 2. Regime Identification and Distant Tail Variability," J. Geophys. Res., **103**, 23503 – 23520, 1998.

[10] Tsyganenko, N. A., "A Magnetospheric Magnetic Field Model With a Warped Tail Current Sheet," Planet. Space Sci., **37**, 5 – 20, 1989.

[11] Tsyganenko, N. A., "Modeling the Earth's Magnetospheric Magnetic Field Confined Within a Realistic Magnetopause," J. Geophys. Res., **100**, 5599 – 5612, 1995.

[12] Nishida, A., "Geotail Mission: Accomplishments and Prospects," in *Sun-Earth Plasma Connections*, Geophysical Monograph 109, (ed. By Burch, Carovillano, and Antiochos), American Geophysical Union, Washington, D.C., pp. 19 – 30, 1999.

[13] Belcher, J. W., A. J. Lazarus, R. L. McNutt, Jr., and G. S. Gordon, "Solar Wind Conditions in the Outer Heliosphere and the Distance to the Termination Shock," J. Geophys. Res., **98**, 2177, 1993.

[14] Smith, E. J., and A. Barnes, "Spatial Dependences in the Distant Solar Wind: Pioneers 10 and 11," p. 521 in *NASA CP 2280, Solar Wind 5*, 1983.

[15] Cravens, T. E., *Physics of Solar System Plasmas*, Cambridge University Press, Atmospheric and Space Science Series, 1997.

[16] Feldman W. C., J. R. Asbridge, S. J. Bame, and J. T. Gosling, "Plasma and Magnetic Fields from the Sun," in *The Solar Output and its Variation*, (ed.) Oran R. White, Colorado Associated University Press, Boulder, 1977.

[17] Geiss, J., and P. Bochsler, "Solar Wind Composition and What We Expect to Learn from Out-of-Ecliptic Measurements," in *The Sun and the Heliosphere in Three Dimensions*, pp. 173 – 186, (ed.) R.G. Marsden, D. Reidel Pub. Co., 1986.

[18] Baker, D. N., and T. I. Pulkinnen, "Large-Scale Structure of the Magnetosphere," in *New Perspectives on the Earth's Magnetotail,* AGU Monograph 105, (ed. by A. Nishida, D. N. Baker, and S. W. H. Cowley), American Geophysical Union, Washington, D.C., pp. 21 – 31, 1998.

[19] Burlaga, L. F., and K. W. Ogilvie, "Heating of the Solar Wind," Astrophys. J., **159**, 659, 1970.

[20] Burlaga, L. F., and K. W. Ogilvie, "Solar Wind Temperature and Speed," J. Geophys. Res., **78**, 2028, 1973.

[21] Purvis, Carolyn K., *Design Guidelines for Assessing and Controlling Spacecraft Charging Effects*, NASA Technical Paper 2361, 1984.

[22] Frank, L. A., and W. R. Paterson, "Survey of Electron and Ion Bulk Flows in the Distant Magnetotail with the Geotail Spacecraft," Geophys. Res. Lett., **21**, 2963 – 2966, 1994.

[23] Paterson, W. R., and L. A. Frank, "Survey of Plasma Parameters in the Deep Geomagnetic Tail: Properties of Plasmoids and the Postplasmoid Plasma Sheet," J. Geophys. Res., **89**, 8872 – 8876, 1984.

[24] Richardson, David L., "Analytic Construction of Periodic Orbits About the Collinear Points," Celestial Mechanics, **22**, 241 – 253, 1980.

[25] Farquhar, Robert W., *The Control and Use of Libration-Point Satellites*, NASA TR R-346, 1970.

[26] Richardson, I. G., C. J. Owen, J. A. Slavin, and T. T. von Rosenvinge, "Energetic (>0.2 MeV) Electron Bursts Observed by ISEE-3 in the Deep (<240 R_E) Geomagnetic Tail," J. Geophys. Res., **98**, 13441 – 13451, 1993.

[27] Hastings, D., and H. Garrett, *Spacecraft-Environment Interactions*, Cambridge Atmospheric and Space Science Series, Cambridge University Press, New York, 1996.

[28] Reames, D., "Energetic Particles and the Structure of Coronal Mass Ejections," in *Coronal Mass Ejections*, Geophysical Monograph 99, (ed. by N. Crooker, J.A. Joselyn, and J. Feynman), American Geophysical Union, Washington, D.C., pp. 217 – 226, 1997.

[29] Gloeckler, G., M. Scholer, F. M. Ipavich, D. Hovestadt, B. Klecker, and A. B. Galvin, "Abundances and Spectra of Suprathermal H+, He++ and Heavy Ions in a Fast Moving Plasma Structure (Plasmoid) in the Distant Tail," Geophys. Res. Letters, **11**, 603 – 606, 1984.

[30] Christon, S. P., G. Gloeckler, D. J. Williams, T. Mukai, R. W. McEntire, C. Jacquey, V. Angelopoulous, A. T. Y. Lui, S. Kokubun, D. H. Fairfield, M. Hirahara, and T. Yamamoto, "Energetic Atomic and Molecular Ions of Ionospheric Origin Observed in Distant Magnetotail Flow-Reversal Events," Geophys. Res. Letters, **21**, 3023 – 3026, 1994.

V. HIGH-ENERGY RADIATION ENVIRONMENT

This section provides an overview of the high-energy radiation environment at the Sun/Earth-Moon L2 libration point. Typically the analysis of the high-energy particle environment includes a quantification of species arising from nominal and extreme solar activity (protons, electrons, and heavy ions), those from extra-solar sources (protons and heavy ions), and those of geomagnetically trapped origin (protons and electrons). Since L2 lies outside the Earth's trapped radiation belts, the specific transfer trajectory of a spacecraft to this libration point will determine its exposure to the trapped radiation.

High-energy particles are capable of penetrating spacecraft shielding materials and directly affecting the operation of electronic components within the vehicle. They may induce the production of secondary species that are capable of reducing the operational lifetime of spacecraft electronics as well as causing immediate data loss or damage. These particles also contribute to the degradation of materials, such as darkening of optical glass, embrittlement of thin film polymers used in thermal insulation, and decreasing the output of solar cells.

The effect of the high-energy particle environment on electronic components must be determined by a comprehensive review of electronic parts selection, circuit design, system design, and software development. Cumulative damage may degrade component operation to such an extent that circuit failure will result. High-energy ionizing particles may trigger parasitic conduction paths within the components themselves, which cause catastrophic, immediate failure. The introduction of free carriers from direct ionization may reduce signal-to-noise margins to the point of data loss. This applies to processing and memory devices and to detector arrays. In order to establish the likelihood of a catastrophic event, or to predict the rate of performance degradation, the high-energy particle fluxes and fluences must be determined. Based upon spacecraft geometry and materials selection, a transport analysis must be performed to establish the degree to which the particles are attenuated prior to reaching internal circuitry, instrumentation, or sensitive materials.

In this chapter, extreme, or "worst-case," conditions are considered, under the rationale that if spacecraft systems are designed to withstand these conditions they will have no problem surviving more benign environments.

5.1 The Natural Space Environment

The natural radiation environment experienced by spacecraft at the libration points is composed of galactic and solar components. The galactic cosmic ray (GCR) element arises primarily from protons and energetic ionized nuclei originating from outside the solar system. GCR are characterized by an omnidirectional flux of approximately 85% protons, 14% alphas, and 1% heavier ions [1]. From an equipment reliability perspective, GCR with energies in the 10^6 electron volts (MeV) to 10^9 electron volts (GeV) range are of most concern. In addition, there is an extremely low flux of GCR with energies that exceed 10^{12} electron volts (TeV). At the higher energies, spacecraft shielding is ineffective in attenuating the particle flux.

Solar flares and coronal mass ejections (CMEs) are eruptive events that may result from solar magnetohydrodynamic instabilities. The precise relationship between these events is still a matter of scientific debate, but this is unimportant for our purposes. Following these eruptive events, large quantities of protons and heavier ions are typically observed. Solar eruptive events are most probable within two years before and four years after solar maximum. These events may affect the particle flux for periods of from several hours to more than a week, but typically do so for two or three days. An example of the solar proton fluence as a function of kinetic energy is presented in Figure 5.1, obtained by integrating the solar proton flux for one year using the JPL 1991 model for 90% worst case conditions [2]. A single eruptive event during this period provided nearly all of the proton flux. The solar proton flux exceeds the GCR flux and typically dominates long-term degradation of spacecraft performance.

A high flux of heavy ions may be observed following a solar eruptive event. These ions are typically lower in energy than galactic cosmic rays but their flux is substantially higher. During major solar events, the flux of some heavy ions may increase drastically, exceeding the GCR background by factors of $10^3 - 10^4$ for short time periods of time [3 – 6]. The damage produced by these particles is a consequence of the particles' ability to ionize the material through which they pass. Therefore, one often describes an energetic, charged species in terms of its linear energy transfer (LET). This is a direct measurement of the amount of energy transferred to the material, and its relationship to the kinetic energy of the particle is well known . The relationship between linear energy transfer (LET) and fluxes of the GCR background and short-duration solar eruptive events are shown in Table 5.1. This table was produced from results of the CREME96 model. In it the GCR prediction was performed for solar maximum and solar minimum, and the solar flux was obtained from the worst day solar model. The model used all elements through Uranium and no geomagnetic shield. The solar heavy ion flux is three to four orders of magnitude greater than the GCR flux at a given LET.

Table 5.1 Galactic cosmic ray integral flux during solar maximum and minimum, and solar heavy ion integral flux following a solar ejection event, as predicted by CREME96.

LET (MeV-cm^2/mg)	GCR Solar Maximum (Particles/cm^2-s)	GCR Solar Minimum (Particles/cm^2-s)	Worst Week Solar Flux (Particles/cm^2-s)
1.01E-01	6.89E+01	9.24E+01	5.40E+04
3.01E-01	5.53E+00	9.92E+00	3.39E+03
5.01E-01	3.85E+00	6.21E+00	1.84E+03
7.01E-01	8.91E-01	2.41E+00	3.76E+02
9.04E-01	6.89E-01	2.00E+00	3.19E+02
1.00E+00	6.50E-01	1.88E+00	3.18E+02
3.02E+00	2.52E-01	6.07E-01	2.73E+02
5.03E+00	1.48E-01	2.77E-01	1.93E+02
7.04E+00	6.11E-02	1.10E-01	1.19E+02
1.01E+01	4.25E-02	6.43E-02	8.72E+01
1.51E+01	1.24E-02	2.12E-02	4.06E+01
2.00E+01	1.09E-02	1.63E-02	3.11E+01
2.52E+01	7.22E-03	9.89E-03	2.19E+01
3.00E+01	1.26E-04	1.65E-04	3.53E-01
3.53E+01	1.24E-06	2.10E-06	5.79E-03
4.01E+01	6.48E-07	1.15E-06	2.38E-03
4.50E+01	3.55E-07	6.54E-07	1.35E-03
5.06E+01	2.57E-07	4.70E-07	1.11E-03
6.02E+01	1.12E-07	2.16E-07	3.96E-04
7.08E+01	4.52E-08	9.17E-08	2.16E-04
8.04E+01	1.25E-08	3.28E-08	1.22E-04
9.03E+01	9.24E-10	3.29E-09	2.15E-05
1.00E+02	3.92E-11	1.69E-10	4.46E-07

The pace of solar eruptive activity correlates with the sunspot cycle. The cycle lasts approximately 11 years, with a 2-year rise to solar maximum, a year at maximum, and a 4-year decline to solar minimum, which lasts about 4 years. The higher degree of solar wind turbulence during solar maximum tends to scatter the GCR and so reduces GCR flux, by up to a factor of 10^3 in some cases. Thus variations in the intensity of the particle fluxes from GCR and from solar eruptions have opposite phases. Figure 5.2 compares the integral fluence of both types of radiation for a ten-year mission. The solar fluence was predicted with the JPL 1991 model for 7 years at 90% worst case. The GCR was predicted with CREME96 using 7 years at solar maximum and 3 years at solar minimum. The geomagnetic shield factor was set to zero for both calculations. For a mission during those years, the fluence of solar ions is considerably higher, but the GCR has significantly higher energies. Because of the strong influence of the solar cycle on the radiation environment, timing of the launch with respect to this cycle and the expected duration of the mission will be important considerations for mission planning and spacecraft design [7].
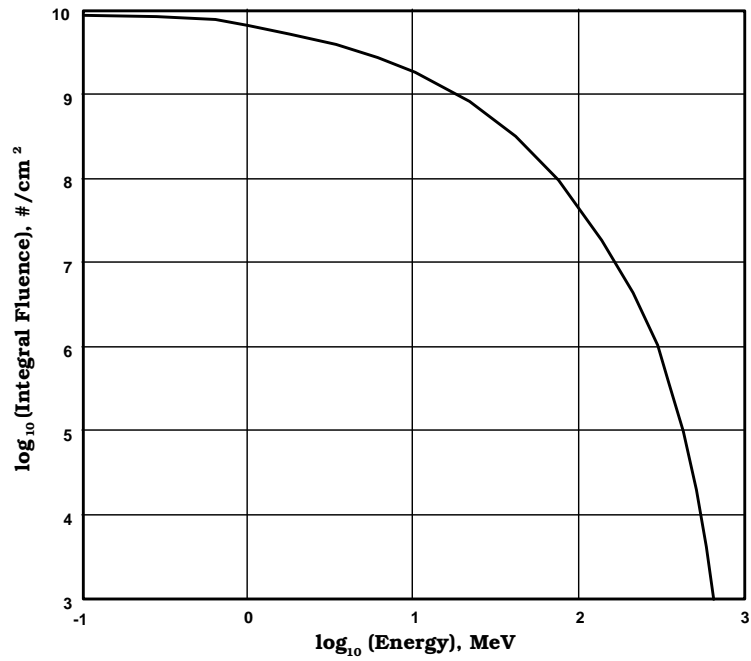
Figure 5.1. Solar proton spectrum predicted by the JPL 91 model, using a 90% worst case probability for a mission of one year's duration during solar maximum.
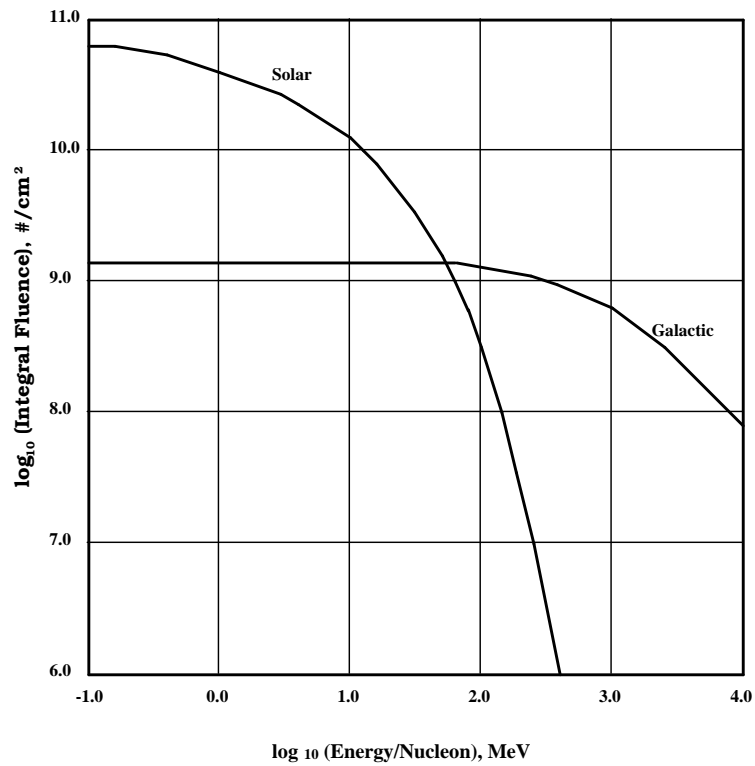

Figure 5.2 Ion spectra for 10 years at L2 for solar and galactic sources.

5.2 Damage mechanisms

5.2.1 Electronics

The effects of radiation on electronics, including processing, memory, and detection devices, can be broadly classified into immediate and long-term. Immediate failures arise from single particles and are termed "single events." They may be non-catastrophic to the part, such as the inversion of a single data bit, or may lead to permanent functional failure, such as the thermal destruction of the part resulting from the activation of parasitic current paths. Generally, single event effects (SEE) are caused by energetic heavy ions but may also occur from nuclear spallation reactions and in some instances from direct ionization by protons. Long-term failures arise from cumulative damage to the crystal lattice of the semiconductor or to charge trapping in amorphous regions. Continuous exposure to the radiation environment may gradually modify device parameters until they exceed the tolerances of the circuit design. Protons, heavy ions, and photons are all potential contributors to long-term performance degradation [8 - 10]. Soft error SEE are often easily mitigated through careful circuit, system, and software design. Hard error and catastrophic SEE may often be reduced by the judicious selection of parts which have been either designed to be resistant to radiation or are intrinsically immune. Actions to minimize or eliminate these failure types can have a large impact on cost and should be carefully considered during budgeting.

Long term effects arise from a total ionizing dose (TID) component and a non-ionizing energy loss component (NIEL). Both arise from the cumulative effect of long exposures of electronic devices to particle and/or photon radiation. Although certain categories of devices show greater propensity to failure from TID or NIEL, the point at which functional or parametric failure occurs can not be predicted and must be determined by testing.

5.2.2 Other Materials

Typical material effects produced by prolonged exposure to ionizing radiation include significant embrittlement, loss of ultimate tensile strength, and an increase in surface hardness. These effects are more pronounced at surfaces, and diminish with depth into a material due to the attenuation of the particle flux.

Energetic electrons have only a limited penetration ability, and tend to dominate the TID in the first few millimeters of external surfaces. The electron dose has been shown to cause damage from as low as 10^5 rads in stressed fluoro-polymers, such as Teflon, while doses above 10^7 rads cause degradation of material properties in most polymers [11].

High-energy protons have much greater penetration depths than electrons, but they do not have a high LET rate until they are either captured or their total energy drops below 100 keV. So while each of the high-energy protons has more energy to deposit in a material, it will spread that energy over a much larger range than the electrons, effectively reducing the amount of energy deposited in a thin film. However, these particles will penetrate very deeply into a material – the average penetration depth for protons above 10 MeV is greater than 254 μm (10 mils). Highly stressed electronic circuits and optical devices may be affected by doses of 10^3 – 10^4 rads, but no damage has been shown to polymers or other insulation materials in that range [11].

Polymeric materials, which rely on long-chain chemical bonds for their physical characteristics, are subject to degradation due to having these bonds broken by high-energy particle penetrations. The resulting 'hanging bonds' then relink with their near neighbors that are subsequently produced by other penetrations, producing short-chain polymers. The result is embrittlement, loss of strength of the material, and the possible degradation of electrical and thermal insulation properties. These degradation effects may have important consequences for the aging NGST sunshield, especially when compounded by the effects of intense UV radiation on the Sun side layer, extreme cold on the shaded side layers, and penetrations by micrometeoroids.

Crystalline materials, such as most metals, rely on the intra- and inter-crystal bonding for their material characteristics. Lattice defects and atomic displacements produced by penetrations by energetic

particles may break or weaken these bonds. In addition, displacements produce a hardening of the material, especially in the surface layers. Ultimately this hardening effect results in embrittlement, and consequent loss of strength. This may have important consequences for metallic elements of the NGST, especially mirror elements, which are intended to be flexible, with reflecting surfaces adjusted by microactuators. Actuation of a cold, embrittled element may have unintended results.

Amorphous materials, such as glasses, may be embrittled as well. The energy introduced by the penetrating radiation may promote the formation of minute crystals in the material, thus altering the bulk properties. It seems clear that an extensive test program will be necessary to characterize the response of all types of candidate NGST materials to combined effects of extreme cold and exposure to high-energy radiation.

5.3 Shielding

GCR are the dominant concern in the case of well-shielded parts, that is, those separated by a significant mass from the outside environment. Energetic GCR can pass through larger thicknesses of shielding with less attenuation than solar ions would experience when penetrating the same mass. Figure 5.3 is a plot of the ionizing dose in silicon as a function of shielding thickness of aluminum for both solar and galactic cosmic radiation [12]. Solar protons are the primary component of dose for a shielding thickness of less than 10 centimeters (which accounts for almost all elements of real spacecraft). GCR ionizing dose is relatively insensitive to increases in shielding thickness. This is important for SEE as well as TID evaluation.

5.4 Conclusion

The high-energy particle environment at L2 is driven by the solar cycle. The impact of the radiation environment on cost will largely be determined by the launch and operation time in relation to the solar cycle, as well as the mass properties of the spacecraft. Maximizing the amount of mass shielding between the electronic components and the external environment will reduce TID damage. Since TID is a cumulative effect, the level of radiation hardness will be established by the mission duration. In order to quantify the expected TID, the spacecraft mass and material properties must be known. However, first order approximations may be used to provide conservative estimates.

Because of the ineffectiveness of shielding against GCR-induced SEE, special consideration will have to be given to the selection of parts and software during the design process. The rapid advancement of technology, shrinking military budgets, and the move to use of commercial off the shelf (COTS) parts have all lead to a sharp reduction in the number of vendors supplying radiation-hardened parts. Cost and schedule impacts regarding radiation testing should be considered and expected if spacecraft reliability and performance requirements are to be adequately ensured and/or quantified. Similarly, materials and components to be used in thermal, optical, power generation, and other roles must be selected with a view to their ability to minimize or withstand the effects of ionizing radiation.
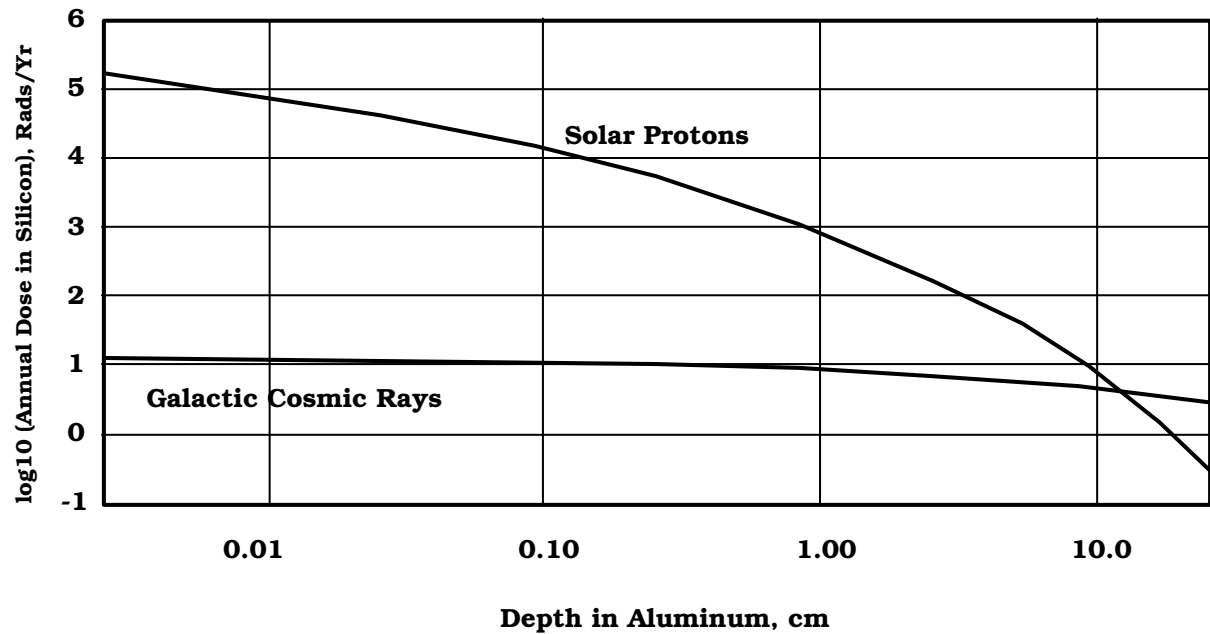
Figure 5.3 Dose vs. depth in aluminum for solar protons and galactic cosmic rays.

References:

[1] J. H. Adams, R. Silverberg, and C. H. Tsao, *Cosmic Ray Effects on Microelectronics, Part II; The Near Earth Particle Environment*, NRL Memorandum Report 4506, August 25, 1981.

[2] J. Feynman, G. Spitale, J. Wang, and S. Gabriel "Interplanetary Proton Fluence of Model: JPL 1991," J. Geophys. Res., **98**, 13281-13294 (1993).

[3] James H. Adams, Jr., *Cosmic Ray Effects on Micro-Electronics (CREME)*, *Part IV*, Naval Research Laboratory Memorandum Report 5901, December 31, 1986.

[4] A.J. Tylka, William F. Dietrich, Paul R. Boberg, Edward C. Smith, James H. Adams, Jr., "Single Event Upsets Caused by Solar Energetic Heavy Ions" , IEEE Transactions on Nuclear Science **43**, 2758-2766 (1996).

[5] A.J. Tylka, James H. Adams, Jr., Paul R. Boberg, Buddy Brownstein, William F. Dietrich, Erwin O. Flueckiger, Edward L. Petersen, Margaret A. Shea, Don F. Smart, and Edward C. Smith, "CREME96: A Revision of the Cosmic Ray Effects on Micro Electronics Code", IEEE Transactions on Nuclear Science, **44**, 2150-2160 (1997).

[6] A.J. Tylka, W.F. Dietrich, and P.R. Boberg, "Probability Distributions of High-Energy Solar-Heavy Ion Fluxes from IMP-8: 1973-1996", IEEE Transactions on Nuclear Science, **44**, 2140-2149 (1997).

[7] H.H. Sauer, R.D. Zwickl, and M. J. Ness, *Summary Data for the Solar Energetic Particle Events of August through December 1989*, NOAA Space Environment Laboratory Report, 21 February 1990.

[8] G.C. Messenger and M.S. Ash, *Single Event Phenomena*, Chapman Hall 1997.

[9] J. C. Pickel & J. T. Blandford, Jr. "Cosmic Ray Induced Errors in MOS Memory Cells," <u>IEEE Trans. Nucl. Sci.</u>, **NS-25**, 1166 – 1171 (1978).

[10] G. Barbottin and A. Vapaille, *Instabilities in Silicon Devices, Volume 3*, First Edition, North-Holland 1999.

[11] R. L. Altstatt and D. L. Edwards, "Modeling Natural Space Ionizing Radiation Effects on External Materials," Proceedings of the SPIE 45th Annual Meeting, July 30 – August 4, 2000, San Diego, CA.

[12] S. M. Seltzer, *Shieldose: Code System for Space Shielding Radiation Dose Calculations*, ORNL/RSIC CCC-379 (1984).

VI. SOLAR ELECTROMAGNETIC RADIATION
AND THERMAL ENVIRONMENT

The electromagnetic radiation and thermal environment present in the L2 vicinity is primarily that produced by the Sun, and is related to the solar irradiance in the Earth's vicinity by an R^{-2} geometric factor. Unlike the near-Earth orbital environment, light reflected from the Earth and longwave radiation emitted by the Earth make negligible contributions to the near-L2 electromagnetic and thermal environments. Similarly, the impact of manmade radio noise should be minimal, with the solar radio noise dominating and placing constraints on the sizing of the NGST halo orbit. The prime influence the Earth and Moon can have there is the casting of shadows which could impact the solar-powered NGST electrical system. In addition to the solar electromagnetic and thermal environment, radio noise produced by galactic sources and other celestial objects, such as Jupiter, is present. Thermally, deep space acts as an excellent heat sink cavity into which the NGST structure will radiate to achieve its 30 - 70 K design operating temperature.

6.1 Solar Irradiance at L2

The "Solar Constant," the radiation that falls on a unit area of surface normal to the line from the Sun, per unit time, and outside of the atmosphere, at 1 AU has the standard value of 1367 $\pm$ 10 W/m^2 [1], allowing for measurement uncertainties. Allowing for the effect of the eccentricity of the orbit of the Earth-Moon system about the Sun, the mean and extreme irradiance values at L2 are as follows:

	Earth-Sun Distance	L2-Sun Distance	Irradiance at L2
1 AU	149,597,870 km	151,105,517 km	1340 W/m^2
Perihelion	147,095,172	148,577,598	1389
Aphelion	152,100,568	153,633,437	1296

Also, the amount of radiant energy that is emitted by the Sun is known to vary slightly throughout the 11 year solar cycle. The exact amount differs from cycle to cycle but it is estimated to be only a fraction of a percent. Table 6.1 provides standard values of the 1 AU solar spectral irradiance at wavelength and the integrated irradiance from zero to wavelength from 0.260 to 4.000 micrometers. Figure 6.1 plots this data from 0.26 to 2.6 micrometers, together with a 5777 K blackbody spectrum for comparison.

Table 6.1 Solar spectral irradiance and integrated irradiance as functions of wavelength at 1 AU [1].

Wavelength μm	Spectral Irradiance W/m^2-μm	Total Irradiance W/m^2	Wavelength μm	Spectral Irradiance W/m^2-μm	Total Irradiance W/m^2
0.260	127.5	3.5	0.355	1027.0	61.0
0.265	247.5	4.4	0.360	949.0	65.9
0.270	270.5	5.7	0.365	1131.0	71.1
0.275	218.0	6.9	0.370	1149.5	76.8
0.280	189.5	7.9	0.375	1090.5	82.4
0.285	298.5	9.2	0.380	1171.0	88.1
0.290	520.5	11.2	0.385	913.5	93.3
0.295	558.0	13.9	0.390	1131.0	98.4
0.300	528.5	16.6	0.395	987.5	103.7
0.305	560.0	19.3	0.400	1616.0	110.2
0.310	611.0	22.3	0.405	1645.5	118.4
0.315	704.0	25.6	0.410	1706.5	126.8
0.320	738.0	29.2	0.415	1752.0	135.4
0.325	800.0	33.0	0.420	1740.5	144.1
0.330	999.0	37.5	0.425	1681.0	152.7
0.335	900.5	42.3	0.430	1522.0	160.7
0.340	943.0	46.9	0.435	1759.5	168.9
0.345	887.0	51.4	0.440	1784.0	177.8
0.350	956.5	56.0	0.445	1929.0	187.0

Table 6.1 (Cont'd.) Solar spectral irradiance and integrated irradiance as functions of wavelength at 1 AU.

Wavelength μm	Spectral Irradiance W/m^2-μm	Total Irradiance W/m^2	Wavelength μm	Spectral Irradiance W/m^2-μm	Total Irradiance W/m^2
0.450	2070.5	197.0	0.800	1148.5	767.7
0.455	2015.0	207.3	0.810	1113.0	779.0
0.460	2041.0	217.4	0.820	1070.0	789.9
0.465	2004.0	227.5	0.830	1041.0	800.5
0.470	1981.5	237.5	0.840	1020.0	810.8
0.475	2016.5	247.5	0.850	994.0	820.9
0.480	2046.0	257.6	0.860	1002.0	830.8
0.485	1898.5	267.5	0.870	972.0	840.7
0.490	1905.0	277.0	0.880	966.0	850.4
0.495	1963.0	286.7	0.890	945.0	860.0
0.500	1881.0	296.3	0.900	913.0	869.2
0.505	1939.5	305.8	0.910	876.0	878.2
0.510	1941.5	315.5	0.920	841.0	886.8
0.515	1825.0	324.9	0.930	830.0	895.1
0.520	1804.0	334.0	0.940	801.0	903.3
0.525	1886.0	343.2	0.950	778.0	911.2
0.530	1924.0	352.8	0.960	771.0	918.9
0.535	1919.5	362.4	0.970	764.0	926.6
0.540	1865.5	371.8	0.980	769.0	934.3
0.545	1893.0	381.2	0.990	762.0	941.9
0.550	1898.5	390.7	1.000	729.7	949.4
0.555	1880.0	400.2	1.050	666.6	984.3
0.560	1843.5	409.5	1.100	611.1	1016.2
0.565	1853.0	418.7	1.125	575.6	1031.1
0.570	1826.0	427.9	1.150	545.2	1045.1
0.575	1846.5	437.1	1.200	501.6	1071.2
0.580	1837.0	446.3	1.250	463.8	1095.4
0.585	1819.0	455.4	1.300	431.6	1117.8
0.590	1751.5	464.4	1.350	388.6	1138.3
0.595	1785.0	473.2	1.400	354.4	1156.8
0.600	1733.5	482.0	1.450	321.8	1173.7
0.605	1754.5	490.7	1.500	296.8	1189.2
0.610	1716.0	499.4	1.550	272.6	1203.4
0.620	1693.0	516.4	1.600	247.6	1216.4
0.630	1656.0	533.2	1.650	234.0	1228.5
0.640	1638.0	549.7	1.700	213.4	1239.7
0.650	1591.5	565.8	1.750	186.4	1249.7
0.660	1524.0	581.4	1.800	166.6	1258.5
0.670	1510.0	596.6	1.850	147.6	1266.3
0.680	1475.0	611.5	1.900	137.2	1273.5
0.690	1420.5	626.0	1.950	127.8	1280.1
0.700	1431.5	640.2	2.000	114.3	1286.1
0.710	1394.0	654.3	2.100	93.1	1296.5
0.720	1374.0	668.2	2.200	75.6	1305.0
0.730	1361.0	681.9	2.300	63.4	1311.9
0.740	1310.5	695.2	2.400	56.7	1317.9
0.750	1271.0	708.1	2.500	48.3	1323.1
0.760	1226.5	720.6	2.600	41.9	1327.7
0.770	1190.0	732.7	2.700	36.5	1331.6
0.780	1182.0	744.6	2.800	31.9	1335.0
0.790	1150.0	756.2	2.900	28.1	1338.0

Table 6.1 (Cont'd.) Solar spectral irradiance and integrated irradiance as functions of wavelength at 1 AU.

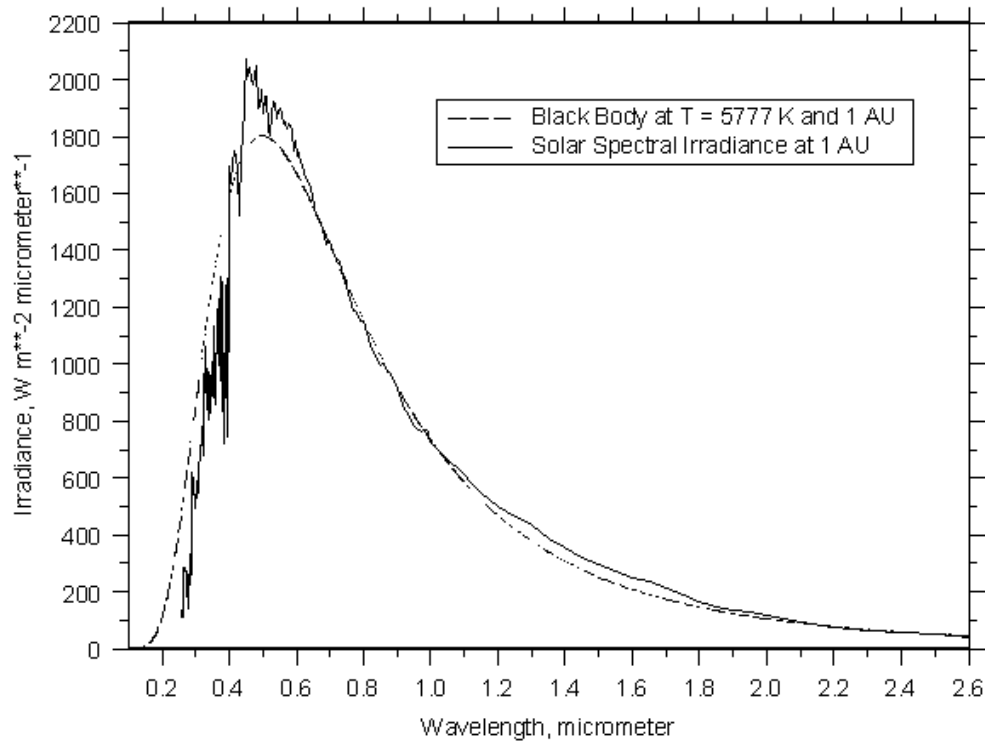| Wavelength μm	Spectral Irradiance W/m^2-μm	Total Irradiance W/m^2
3.000	24.8	1340.6
3.100	21.8	1343.0
3.200	19.6	1345.0
3.300	17.4	1346.9
3.400	15.7	1348.5
3.500	14.1	1350.0
3.600	12.8	1351.4
3.700	11.5	1352.6
3.800	10.4	1353.7
3.900	9.4	1354.7
4.000	8.6	1355.6

Figure 6.1 Solar spectral irradiance vs. wavelength, and black body comparison.

6.2 Earth and Moon

6.2.1 Illumination and Heating

Excluding the Sun, the Earth and Moon are the only significant sources of illumination, planets, stars, and other celestial objects being feeble in comparison. The light from the Earth and Moon will be forward-scattered sunlight from the illuminated crescents visible from the L2 halo orbit. If we consider the spacecraft to be at one of the maximum-Y extensions of the rather large halo orbit shown in Figure 6.2, at a
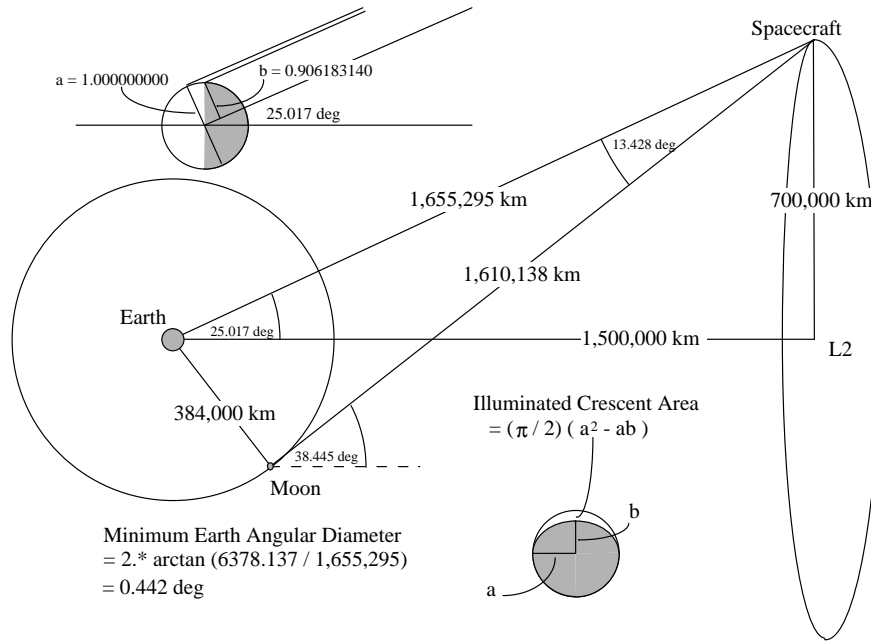
Figure 6.2 Earth angular size and illuminated crescent calculations at the farthest location on an example large halo orbit about L2.

position of (1,500,000 km;700,000 km;0 km) in the rotating coordinate frame with origin at the Earth-Moon barycenter, then the disc of the Earth will subtend an angle of approximately 0.442 degrees or an area of 0.153 square degrees. Of this disc, the illuminated portion will comprise a crescent having only 4.7% of the total area, or 0.0072 square degrees. Albedo radiation is about 0.007 ± 0.001 W m^{-2} from the full disc Earth seen at L1, but at the L2 position Earth albedo radiation will be 0.0004 W m^{-2} or less. In the case of the Moon, the maximum illuminated crescent area to be seen from our vantage point is 0.0013 square degrees, and the lunar contribution will be ≤ 0.0002 W m^{-2}. These objects will be negligibly small contributors to the local NGST illumination, but may be significant stray light sources for optical detectors.

At closest approach in the above halo orbit, Earth will subtend 0.546 degrees or an area of 0.234 square degrees, with a visible illuminated crescent of 0.0040 square degrees, and it is at this point that it will give its maximum in thermal infrared radiation. For the Earth the longwave radiation is only 0.004 ± 0.001 W m^{-2}. At its closest point the Moon will subtend 0.208 degrees or an area of 0.034 square degrees, with a visible illuminated crescent of 0.0008 square degrees. Approximate effective blackbody temperatures are 255 K for the Earth and 273 K for the Moon.

6.2.2 Eclipses

While the Earth and Moon will not be significant light or heat sources they will cast shadows that occupy portions of space near L2. If uninterrupted electrical power is a priority, the NGST halo orbit must be sized to avoid these eclipse zones. For the barycenter at 1 AU, the angular size of the Sun seen from L2 is 0.526 degrees, while the angular sizes of the Earth and Moon are 0.487 degrees and 0.133 degrees, respectively. Thus any eclipses will be at most annular, not total. Still, a central annular eclipse due to the

Earth would block about 80% of the solar illumination, and the eclipse duration could be several days, owing to the slow relative motion of the spacecraft in its halo orbit.

Due to the variation of the plane of the Earth-Moon system with respect to the ecliptic, and the monthly revolution of the bodies, rectangular avoidance zones are projected on the plane of the sky where eclipses could occur. In Figure 6.3 we are looking along the line of sight from the Earth-Moon barycenter toward L2. The zone where the Earth shadow must be avoided is about 22,000 km wide and 14,000 km high at L2, and would doubtless be avoided for any reasonably large halo orbit. The Moon shadow avoidance zone is about 777,000 km wide and 73,000 km high. Any requirement to avoid Moon eclipses will set a minimum on the allowable amplitudes of the halo orbit.
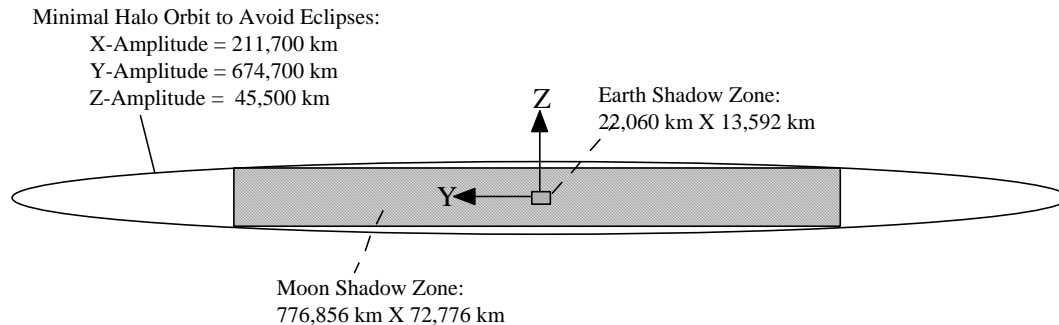
Minimal Halo Orbit to Avoid Eclipses:
    X-Amplitude = 211,700 km
    Y-Amplitude = 674,700 km
    Z-Amplitude = 45,500 km

Earth Shadow Zone:
22,060 km X 13,592 km

Moon Shadow Zone:
776,856 km X 72,776 km

Figure 6.3 L2 zones where eclipses are possible, and minimum halo orbit to avoid them.

6.3 Radio Noise

Several sources of radio noise are present which may interfere with communications with the NGST or cause other instrumental interference. These sources include galactic radio noise, solar and other natural radio noise, and manmade radio noise from the Earth.

6.3.1 Galactic Radio Noise

Galactic radio noise extends from 15MHz to 100 GHz [1]. There are numerous sources, but they aggregate into a general emission that is broadly directional toward and perpendicular to the galactic plane, and which varies by about 10 dBW/Hz. This noise will be an important factor in communications between 40 and 250 MHz. Figure 6.4 presents levels of galactic radio noise as a function of frequency.

6.3.2 Solar and Other Natural Radio Noise

The Sun produces radio noise that can interfere with communications. Solar emissions fall into two classes: emission from the quiet Sun and emission from the disturbed Sun. The term "quiet Sun" refers to the absence of sunspots on the solar disc for a period of several months. Quiet Sun emission is the emission which is not associated with any form of solar activity, and may be regarded as the "minimum" or "basic component" solar radiation. Radiation from the disturbed Sun consists of a slowly varying component with maximum energy at 10 to 21 cm wavelength, and a rapidly varying component, generally associated with flares, with an absolute flux density which can have a maximum anywhere from the meter to millimeter range [2]. Figure 6.5 plots these components, and compares them with the radio wavelength portions of blackbody spectra at various temperatures.

Different regions of the Sun are observed at different wavelengths. At millimeter wavelengths, the radiation is from the chromosphere, and its basic component may fluctuate by 5 to 10 percent. In the centimeter range, the quiet Sun radiation is of chromospheric origin, but the corona also contributes a slowly varying component, which may vary on timescales of days, weeks, or months; its intensity is closely correlated with sunspot number. At wavelengths less than 10 cm, the slowly varying component is partly
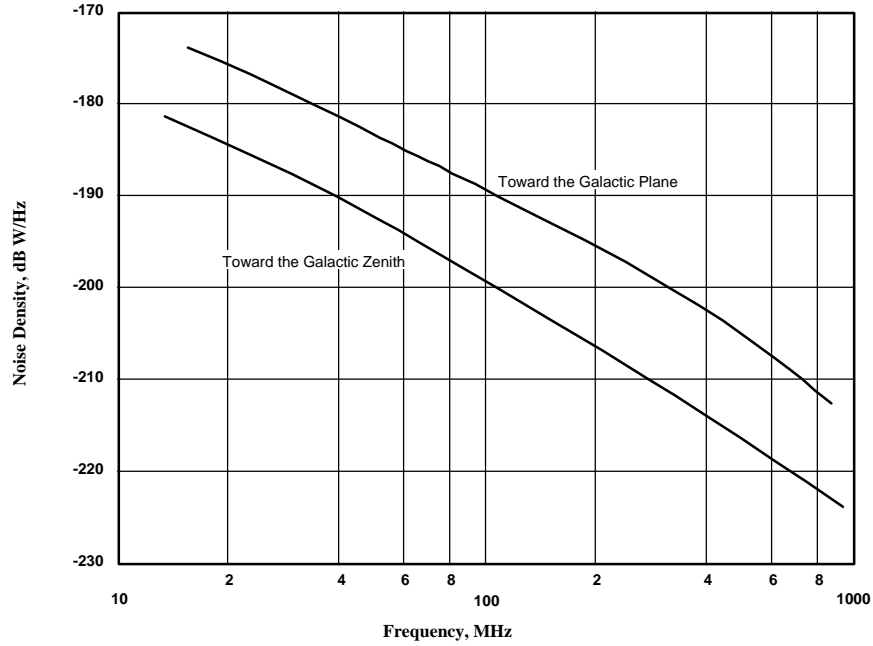
Figure 6.4 Levels of galactic radio noise as a function of frequency [3].

circularly polarized. Decimeter and meter wavelengths are radiated from various heights in the corona. At meter wavelengths the observed radiation comes from heights ranging from 100,000 to 200,000 km above the photosphere. This radiation is subject to much burst activity, and the temperature corresponding to its basic component can fluctuate by up to 20 percent about a value of 10^6K. Intense bursts are associated with solar flares and related events. These bursts can produce fluxes as high as 10^{-17} W m^{-2} Hz^{-1}, peaking either in the m, dm, cm, or mm ranges, depending on the nature of the burst. The degree of modulation of the
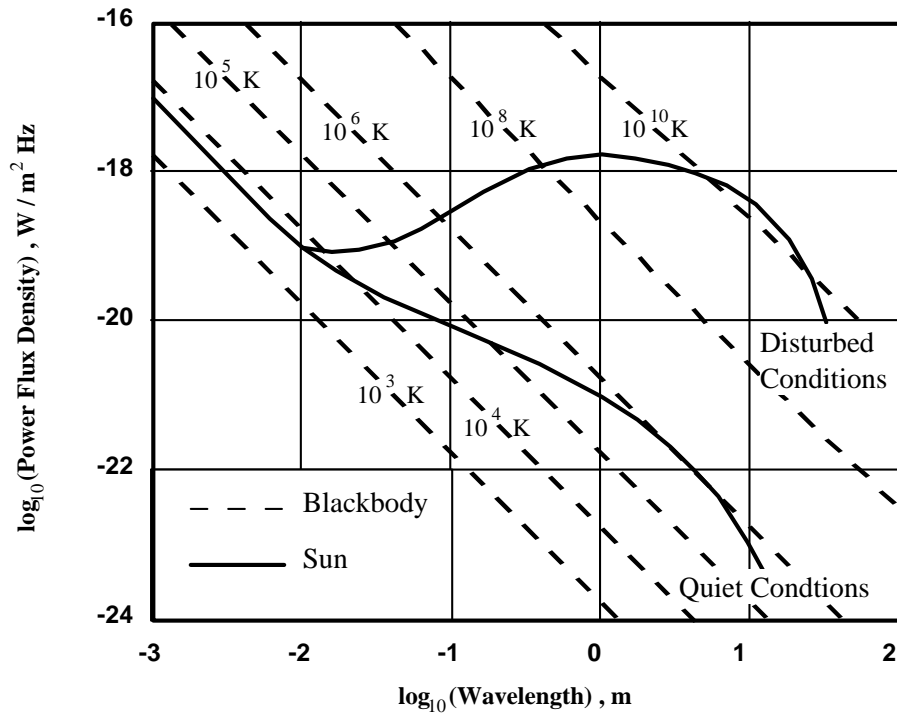

Figure 6.5 Comparison of solar spectra and blackbody spectra at various temperatures.

51

Sun's radio flux at L2 produced by bursts diminishes as wavelength decreases. The burst component maybe many orders of magnitude larger than the quiet Sun radio flux at L2 at meter wavelengths, but even the largest bursts only change the total flux at millimeter wavelengths by a factor of less than 2.

Because of the solar radio noise, the NGST halo orbit must be sized so that the angle between the lines of sight to the Earth and to the Sun is greater than some limiting value. For the WIND mission, this limiting angle was set at 5 degrees [4]. Using this limit, the minimum Z-amplitude of the halo orbit should be $\pm$ 151,000 km; owing to the connection between the amplitudes, the corresponding minimum X- and Y-amplitudes should be $\pm$ 217,000 km and $\pm$ 692,000 km, respectively.

Magnetospheric and solar wind plasmas may generate emissions at frequencies from 1 to 10 MHz down to direct current. The electron plasma frequency is found from the electron density as [3]

$$f_p = | \, n_e \, e^2 \, / \, m_e \, \pi \, |^{\,1/2} = 0.90 \text{ MHz} \, | \, n_e \, / \, (10^4/\text{cm}^3) \, |^{\,1/2} \qquad (6.1)$$

where n_e is the electron density per cm^3, e^2 is square of the electronic charge, 9.48 x 10^{-9}, and m_e is the electron mass in grams, 9.11 x 10^{-28}. Note that this electron plasma frequency is independent of temperature. Emissions due to external sources with frequencies below the plasma frequency will be severely damped and will not reach the spacecraft [5]. There may be locally generated electrostatic noise at the local plasma frequency.
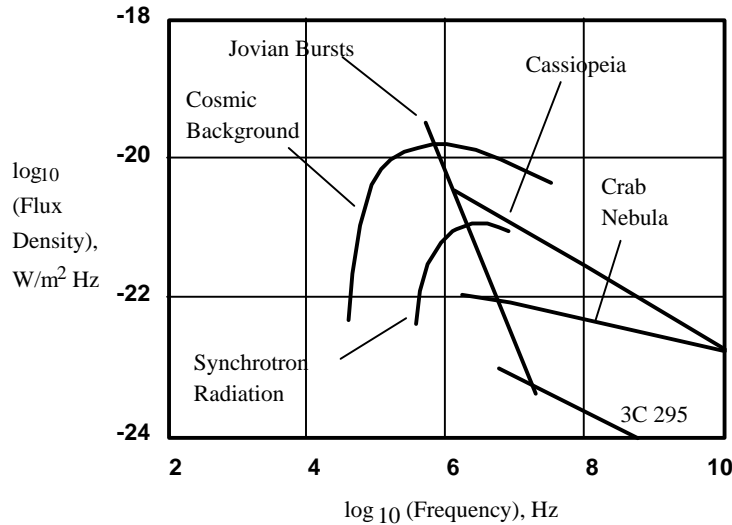

Figure 6.6 Power flux density levels for various frequency ranges
of naturally occurring electromagnetic noise.

As shown in Figure 6.6, various other sources of radio noise exist, including outbursts from Jupiter and continuous noise from supernova remnants, quasars, etc. These sources are either intermittent (notably Jupiter), are of low power level, or both, and they should not cause significant communications difficulties. They could induce noise in some types of detectors, however.

6.3.3 Manmade Radio Noise

Artificial radio noise typically consists of a plethora of narrow-band signals produced by civilian and military communications transmitters, radars, and other electronic devices. Manmade noise below the peak ionospheric plasma frequency of 1 to 10 MHz cannot propagate through the lower ionosphere without significant attenuation; however, narrow-band sources from 1 MHz to 300 GHz may be detectable, since they will get through [3]. An expression for the electric field at a distance r from a radio-frequency transmitter is

$$E = (30 \, \mathit{ERP})^{1/2} / r \qquad\qquad (6.2)$$

where *ERP* is the effective radiated power in watts (product of the transmitter power and antenna gain), *r* is in kilometers, and E is measured in millivolts per meter (*mV* / m). Thus a radar with a power of 10 kW and an antenna gain of 40 dB (factor of 10,000) produces an electric field of approximately 110 *mV* / m at a distance of 500 km (e.g., in LEO), but this declines to only about 37 μV / m at L2. Presumably such a source would have a very narrow beam width (perhaps less than a degree), so only deliberate attempts to signal a spacecraft at L2 are likely to be detected there.

References

[1] F. Kasten and C. G. Justus, *Solar Spectral Irradiance*, International Illumination Commission (CIE) Publication 85., CIE TC2-17 Committee, 1989.

[2] *Handbook of Geophysics and Space Environment*s, Shea L. Valley, Sci. Ed., Air Force Cambridge Research Laboratories, 1965.

[3] Anderson, B. Jeffrey, Ed., Robert E. Smith, Compiler, *Natural Orbital Environment Guidelines for Use in Aerospace Vehicle Development*, NASA Technical Memorandum 4527, Marshall Space Flight Center, June 1994.

[4] P. Sharer, J. Zsoldos, and D. Folta, "Control of Libration Point Orbits Using Lunar Gravity-Assisted Transfer," AAS 93-295, 1993.

[5] *Spacecraft - Environment Interactions*, Daniel Hastings and Henry Garrett, Cambridge University Press, 1996.

VII. METEOROID ENVIRONMENT

Modern analyses of past and new meteoroid data have shown that the current NASA model [1] is in need of revision for two reasons: its assumption that the sporadic background of meteoroids is isotropic is in error, and its estimate of the number of high velocity meteoroids is low by a few orders of magnitude. That the meteoroid background is non-isotropic has been known since 1957 [2], but insufficient data and lack of computer power prevented directionality from being included in the engineering meteor models. The underestimation of the high velocity meteoroids was discovered in the late 1980's during a re-analysis of some old optical and radar data; it has since been confirmed by other researchers using more extensive data sets [2]. The principal quantity the current meteor model appears to get right is the total background flux.

In this chapter we consider the spatial and temporal aspects of the meteoroid environment that are well characterized: the sporadic background and the meteoroid streams. To date very little is known about the physical nature of meteoroids, especially with regard to the details of their composition and density. The conversion of meteor visual magnitude and velocity to mass is also quite uncertain (by perhaps an order of magnitude at the extremes), and this has serious implications for penetration analyses. Such analyses will be discussed in the third part of the chapter.

7.1 Background or "Sporadic" Meteoroid Environment Description

Any model of the meteoroid environment in the vicinity of L2 must be based on currently available reliable data, all of which is Earth-based, and must properly describe three aspects of the environment: flux, directionality, and velocity distribution.

7.1.1 Flux

As mentioned above, the flux appears to be adequately described by the current model, which was first stated by Grün et al. [1]. Ignoring gravitational focusing and planetary shielding effects (which apply only near Earth), the flux, $F_{Grün}$, of meteoroids m^{-2} yr^{-1} greater than mass m, in grams, on a tumbling or randomly oriented surface is given by:

$$F_{Grün} = c_0 \, [(c_1 \, m^{0.306} + c_2)^{-4.38} + c_3(m + c_4 m^2 + c_5 m^4)^{-0.36} + c_6(m + c_7 m^2)^{-0.85}] \qquad (7.1)$$

where the constants $c_0 \dots c_7$ are

$c_0 = 3.156 \times 10^7$	$c_1 = 2200$	$c_2 = 15$	$c_3 = 1.3 \times 10^{-9}$
$c_4 = 10^{11}$	$c_5 = 10^{27}$	$c_6 = 1.3 \times 10^{-16}$	$c_7 = 10^6$

Equation (7.1), known as the "Grün Equation," is plotted in Figure 7.1. Note that this is an expression for the flux in terms of mass; in order to convert to the particle sizes required by the penetration equations used in the design of shielding, a knowledge of the meteoroid density is required. The mass density for meteoroids spans a wide range, from approximately 0.2 g cm^{-3} or less for cometary dust, to 8 g cm^{-3} for metallic asteroidal fragments. Even values for the average mass density vary widely by source and particle size, so only rough overall mean values can be estimated. Recommended mean values are 2 g cm^{-3} for meteoroids smaller than 10^{-6} g; 1 g cm^{-3} for masses between 10^{-6} and 0.01 g; and 0.5 g cm^{-3} for masses above 0.01 g. For many purposes, the density can be set at approximately that of water, 1.0 g cm^{-3} [3].

7.1.2 Directionality

Most meteor scientists now recognize that background meteors radiate from 6 distinct sources, rather than coming in uniformly from all directions [4]. Imagine a coordinate system in the plane of the Earth's orbit (the ecliptic), with 0º longitude being located at the position of the Sun and 270º being the approximate direction of the Earth's motion. In this system, we would see background meteors radiating from a source near the Sun (the Helion source), a source nearly opposite the Sun (the Anti-Helion source), from two sources near the direction of Earth's velocity (the Apex sources) and from two sources located
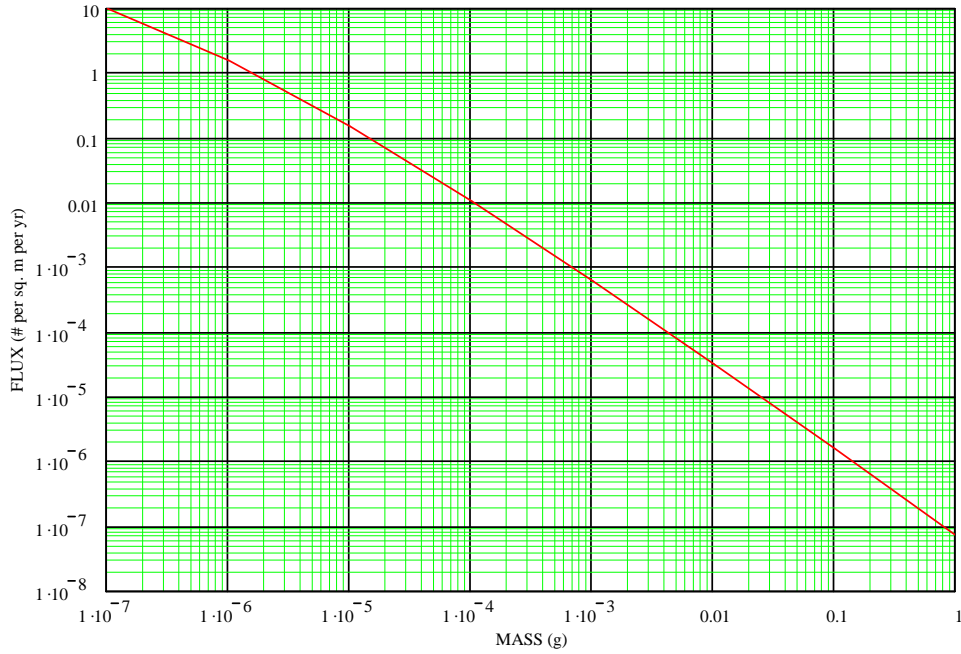
Figure 7.1 Sporadic meteoroid flux as a function of mass (Grün Equation).

towards the Apex, but 60° above and below the plane of the ecliptic (the Toroidal sources). By far the greatest flux of meteors comes from the Helion and Anti-Helion sources, accounting for about 60% of the total flux. The Apex sources provide another 15% each, and the Toroidal sources contribute the final 10%. Table 7.1 summarizes this directionality information. One can use this model to produce an estimate of the flux, f_n, seen by a given spacecraft surface, n, as

$$f_n = \sum_{i=1}^{6} F_{Grun} \int_0^{\pi/2} \int_0^{2\pi} G(\theta,\phi,i)\cos(\phi)d\theta d\phi \qquad (7.2)$$

where $G(\theta,\phi,i)$ is that part of a gaussian flux distribution peaking at radiant i visible from surface n, ϕ is the angle between the normal to the surface and the line of sight, and θ is an azimuthal angle about the normal. (Integrating $G(\theta,\phi,i)$ over all angles reproduces the fraction of the Grün flux due to radiant i seen in Table 7.1.) Summing over all six radiants gives the total flux seen by the surface. These calculations show that Helion- and Anti-Helion-facing surfaces see 50% of the meteor flux, whereas an Apex–oriented surface sees 95%. A surface oriented opposite the Apex is luckiest, as it receives only 5% of the total meteor flux.

7.1.3. Velocity

Unlike with the current model, the six-source description given above requires a minimum of three velocity distributions, assuming symmetry among sources of the same type. Unfortunately, none of these distributions have been published in the literature to date. Even so, it is still possible to determine average velocities for meteors radiating from the six sources [4]. This information is given in Table 7.1. Notice that while the Helion and Toroidal sources have similar average velocities, the Apex meteoroids have an average speed of about 55 km s^{-1}, which is almost twice that of the other sources. As about 30% of the

Table 7.1 Background meteor radiants' characterisitics.

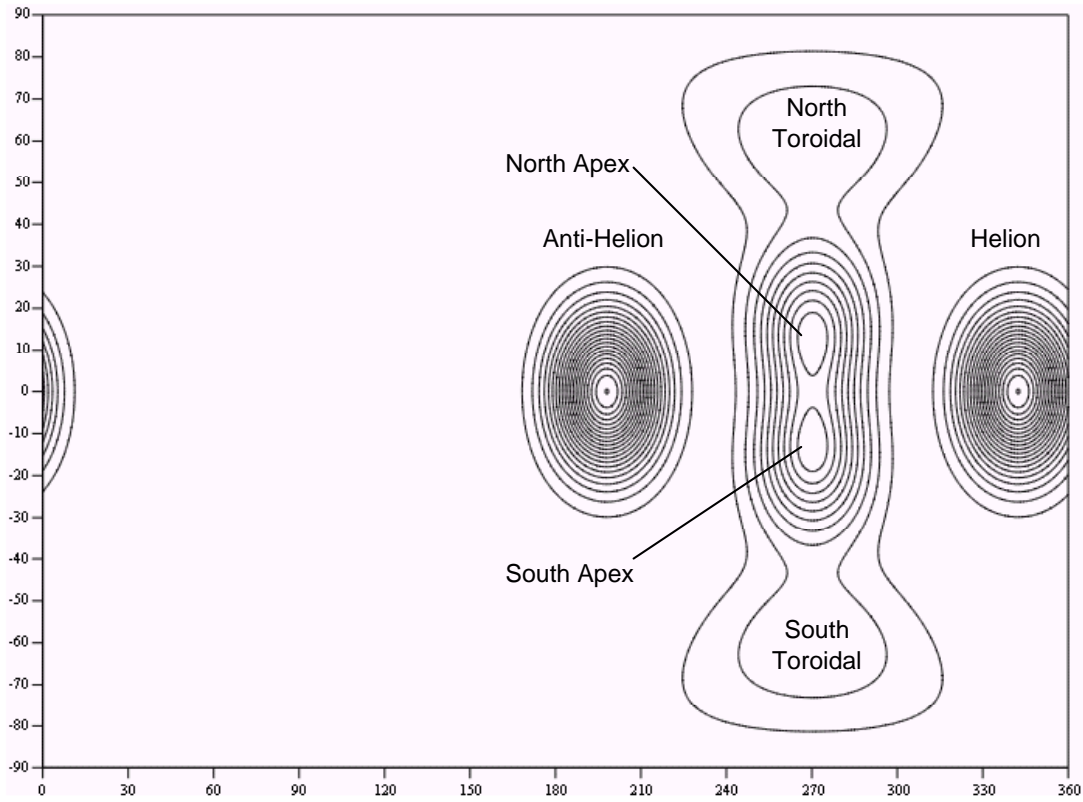| Source	Longitude	Latitude	Fraction of Flux	V_{avg} , km s^{-1}
Helion	342°	0°	.30	29
Anti-Helion	198°	0°	.30	29
North Apex	270°	+15°	.15	55
South Apex	270°	-15°	.15	55
North Toroidal	270°	+60°	.05	35
South Toroidal	270°	-60°	.05	35

Figure 7.2 A Model of the Meteor Sky. The coordinates are ecliptic, with the horizontal axis giving the longitude in degrees from the solar direction (Sun is at 0°, direction of Earth's motion is at 270°) and the vertical, ecliptic latitude.

meteoroid flux comes from the direction of the Apex, this would indicate that some considerations should be given to protecting surfaces that might face in this direction for an extended period of time: Masses being equal, the average Apex meteoroid will have roughly four times the kinetic energy, or "striking power," and sixteen times the plasma production potential (since plasma produced by a meteoroid impact is proportional to v^4) of a meteoroid from the Helion sources. Striking power relates to probability of penetration and the resulting surface and interior damage a spacecraft may sustain, while plasma production may induce static electric discharges, current flows, and other effects that may damage spacecraft electronics.

7.2 Meteoroid Stream Environment Description

In addition to the normal influx of background meteoroids, the Earth (and spacecraft near it) also encounters quasi-periodic meteoritic enhancements, caused by streams of material ejected from short period comets that pass near the Earth's orbit. These streams of debris (which are not included in the Grün model) produce the meteor "showers" observed here on Earth, and normally represent only a modest enhancement of a few percent over the background. However, the column density of material in a stream can be increased by a recent passage of the parent comet through the inner Solar System, thereby resulting in an "enhanced" shower (meteor rates of several hundred per hour) or a meteor "storm" (rates in excess of 1000 meteors per hour). As might be expected, an enhanced shower or storm represents a time of increased risk for spacecraft. Streams that are notorious for producing enhanced showers or storms at Earth are the Perseids, the Draconids, and the Leonids. The Leonids are especially famous for producing spectacular meteor storms at 33-year intervals.

Not only can these streams cause problems in Earth orbit, but they can also pass near the L2 point and increase the risk to spacecraft stationed near it. Figure 7.3 illustrates this point. Based on dynamical calculations performed by Peter Brown [5], the figure shows that there are long periods of enhanced stream activity near L2 in August of 1996 – 2003, and in other years as well. In addition to the column density increase, the speed of the Perseids, about 59 km s^{-1}, translates to greater-than-normal striking power and much greater-than-normal plasma production potential.

Table 7.2 presents information on those meteor streams that are known to have the potential for causing enhanced or storm activity at Earth and L2. Experience shows that some thought should be given to how to deal with stream activity, whether through design or mitigation procedures: At least one spacecraft has been damaged and one effectively killed by encounters with meteor streams. In mid-September of 1967, the Mariner IV spacecraft was located midway between the orbits of Earth and Mars when it encountered an unknown meteor stream. The onboard meteor counter registered a thousand-fold increase in flux for about 45 minutes, during which time the spacecraft was slightly torqued about its roll axis and had some of its thermal insulation ripped away. Mariner IV was lucky in that it suffered no major damage. Such was not the case with the European Olympus communications satellite in August of 1993. During the enhanced Perseid shower experienced that year, Olympus was struck somewhere near its electronics bay. The resulting plasma discharge generated enough current to disable a gyro, causing the satellite to tumble. By the time control was restored some days later, the spacecraft had used practically all of its fuel and was effectively dead as far as its mission was concerned.

Table 7.2 Meteor streams known to produce enhanced or storm level activity.

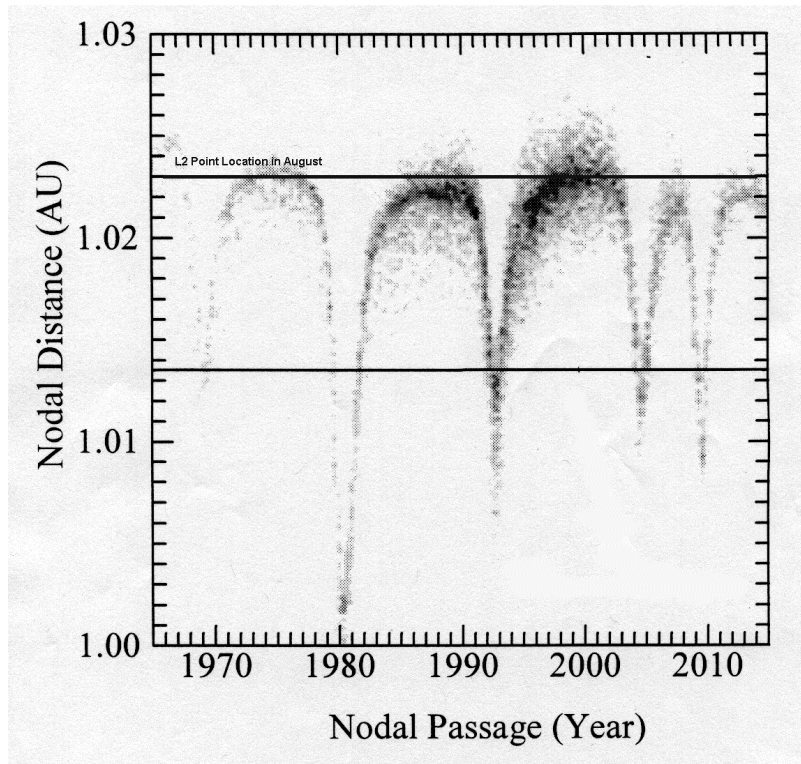| Stream	Radiant		Speed (km s^{-1})	Time of max activity
	RA	Declination		
Quadrantids	230°	+49°	41	Jan 03
κ Cygnids	286°	+59°	25	Aug. 18
Lyrids	271°	+34°	49	Apr. 22
Draconids	262°	+54°	20	Oct. 09
Perseids	46°	+58°	59	Aug 13
Leonids	152°	+22°	71	Nov. 17-18

Figure 7.3 Location of enhancements in Perseid meteor stream column density
during a span of fifty years centered on 1990 [5].

7.3 Penetration Analyses and Associated Error Bounds

In the analysis of a spacecraft design, the probability of no penetration (PNP) is usually taken to be *the* measure of the vulnerability of the spacecraft with respect to the meteoroid and orbital debris environment. However, to be truly informative, probability calculations should take into account the uncertainties associated with the penetration equations and the environment models, thereby producing a PNP number with associated error bounds. To facilitate such an evaluation, we present the following procedure to calculate the upper and lower limits on a given PNP.

7.3.1 Procedure

There are two basic uncertainties that need to be taken into account in calculating a PNP:

1) Uncertainties in environment models: In the case of the standard meteor model specified in NASA TM 4527 [3] and elsewhere, the uncertainty can be separated into two parts – the uncertainty in the flux of particles of a given mass (for particles with masses less than 1 μg), and the uncertainty in the mass for a given flux (applies to larger particles). It is generally accepted that the environment models are uncertain to at least a factor of 2 in these respects.

2) Uncertainty in values of penetrating masses calculated by penetration equations: Even though these "ballistic limit" masses are based on experimental data, uncertainties in the various equations used to describe a given material configuration yield masses that vary by at least a factor of 3.

We shall assume that the uncertainties are symmetric about the values calculated from the environment model and the penetration equations. In this case,

58

$$F_L = \frac{1}{\sqrt{K_E}} F(\sqrt{K_P} m_P, \ldots) \qquad\qquad F_U = \sqrt{K_E} F(\frac{1}{\sqrt{K_P}} m_P, \ldots)$$

where F_L and F_U are the lower and upper limits on the flux, K_E is the uncertainty in the environment model, and K_P is the penetration equation mass uncertainty. The nominal value of the flux, $\langle F \rangle$, is represented by

$$\langle F \rangle = F(m_P, \ldots)$$

In these circumstances, we can establish the bounds on the number of penetrating hits taken by the spacecraft:

$$N_L = F_L A_s \Delta T \qquad\qquad \langle N \rangle = \langle F \rangle A_s \Delta T \qquad\qquad N_U = F_U A_s \Delta T$$

where A_s is the appropriate spacecraft area, ΔT is the mission duration, N_L is the penetrating hit lower bound, $\langle N \rangle$ is the expected number of hits, and N_U is the upper bound on penetrating impacts. Then the PNP and its associated limits are given by:

$$PNP_B = e^{-N_L} \qquad\qquad \langle PNP \rangle = e^{-\langle N \rangle} \qquad\qquad PNP_W = e^{-N_U}$$

where PNP_B is the best-case PNP, $\langle PNP \rangle$ is the expected PNP, and PNP_W is the worst-case PNP. Given that the K's are chosen appropriately (2 in the case of K_E and 3 in the case of K_P), the above expressions should adequately describe the risk to the spacecraft. If it is desired that the spacecraft be extremely robust, the goal will be to get PNP_W as high as possible, though this is quite likely to prove to be costly and result in a heavy satellite. If the results of the environment models accurately reflect the natural world and if there is a high degree of confidence in the penetration equations used in the analysis, then $\langle PNP \rangle$ should give the best estimate of risk to the vehicle. For all practical purposes, PNP_B should be ignored, as it represents circumstances that almost never occur in nature.

7.3.2 Example

Assume we have a typical LEO satellite with h = 500 km, A_s = 100 m^2, and ΔT = 1 year. Applying the procedure given above results in the dependence of the various PNP's on mass shown below in Figure 7.4. Note that even for nominal PNP values as high as 0.93, the difference between the worst- and best-case PNP is fairly large (~0.17). It is also obvious that one has to achieve a nominal PNP of 0.97 or larger before the worst-case PNP is above 0.90. This figure underscores the point that, for most spacecraft, the PNP calculations are very uncertain and should not be regarded as "hard" numbers. Only projects with a great deal of money and a large weight allowance can achieve PNP's high enough such that the uncertainties are unimportant. The majority of projects must accept uncertain PNP's and hope that the nominal values will indeed apply to their particular mission.

7.4 Summary

The meteoroid environment near L2 is composed of background sporadic meteoroids and meteoroid streams. The sporadic meteoroids emanate from six radiants centered about the direction of revolution of L2 about the Sun: the Helion, Anti-Helion, North Apex, South Apex, North Toroidal, and South Toroidal sources. Stream meteoroids are often associated with known comets' orbits, and enhancements in the fluxes of these meteoroids can be predicted in some cases. While meteoroids are primarily small, and are believed to have lower densities than many orbital debris objects, their higher impact speeds make them a serious penetration concern. Owing to the numerous uncertainties in our knowledge of these objects (mass, density, composition, and size), calculations of probability of no

penetration need to include error bounds if sound design solutions are to be realized for shielding spacecraft components against them, and in predicting spacecraft components' useful lives.
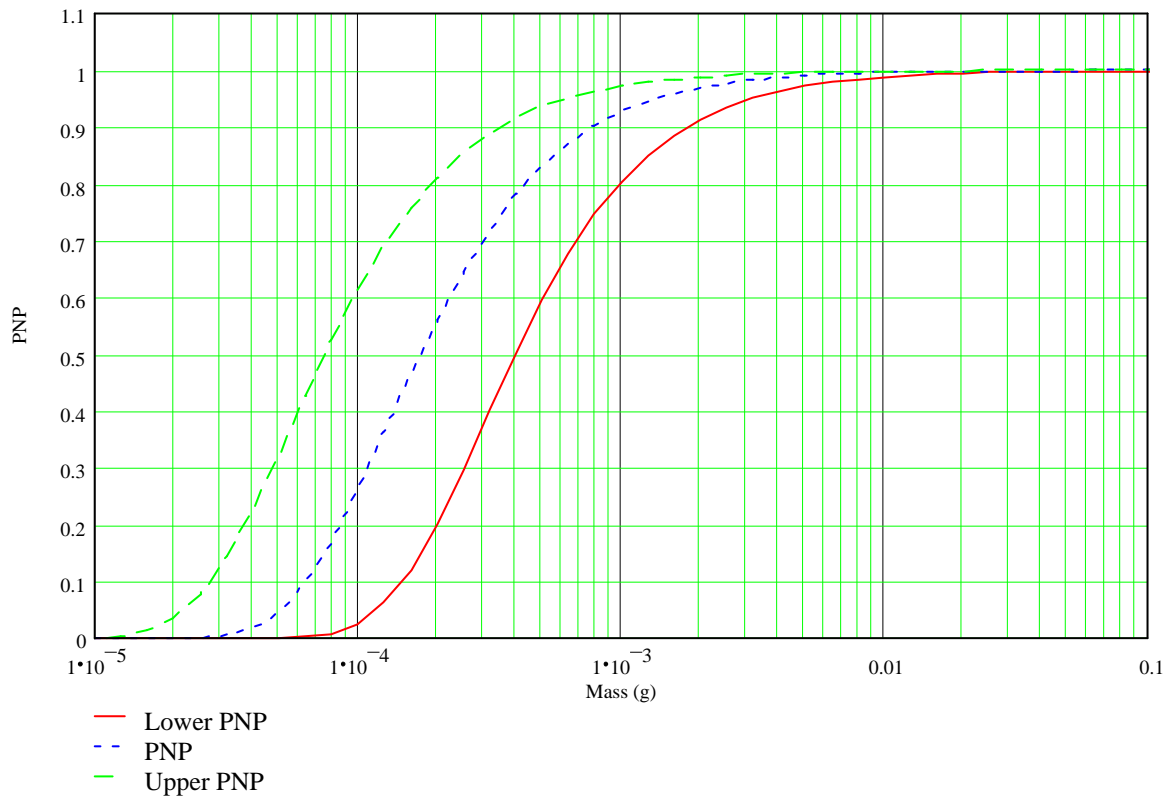

Figure 7.4 Nominal PNP and error bounds: "Lower" is worst-case bound; "Upper" is best-case bound.

References

[1] Grün, E., Zook, H. A., Fechtig, H., and Giese, R. H., "Collisional Balance of the Meteoritic Complex," Icarus, **62**, 244 – 272 (1985).

[2] Taylor, A. and McBride, N., "A Radiant-Resolved Meteoroid Model", *Proceedings of the Second European Conference on Space Debris*, ESOC, Darmstadt, Germany, 17 – 19 March 1997, pp. 375 – 380.

[3] Anderson, B. Jeffrey, Ed., Robert E. Smith, Compiler, *Natural Orbital Environment Guidelines for Use in Aerospace Vehicle Development*, NASA Technical Memorandum 4527, Marshall Space Flight Center, June 1994.

[4] Brown, P. and Jones, J., "A Determination of the Strengths of the Sporadic Radio-Meteor Sources," presented at the *International Conference on Meteoroids* 28-31 August, 1994.

[5] Brown, P., *Personal communication* (1999).